

Inverse modeling of carbon monoxide surface emissions using Climate Monitoring and Diagnostics Laboratory network observations

Gabrielle Pétron,^{1,2} Claire Granier,^{1,3,4} Boris Khattatov,⁵ Jean-Francois Lamarque,⁵ Valery Yudin,⁵ Jean-Francois Müller,⁶ and John Gille⁵

Received 18 September 2001; revised 29 March 2002; accepted 22 April 2002; published 19 December 2002.

[1] A three-dimensional (3-D) inverse modeling scheme is used to constrain the direct surface emissions of carbon monoxide CO. A priori estimates of CO emissions are taken from various inventories and are included in the IMAGES model to compute the distribution of CO. The modeled CO mixing ratios are compared with observations at 39 CMDL stations, averaged over the years 1990–1996. The interannual variability of CO sources is therefore ignored. We show that the method used (time-dependent synthesis inversion) is able to adjust the surface fluxes on a monthly basis in order to improve the agreement between the observed and the modeled CO mixing ratios at the stations. The Earth surface is divided into regions. The spatial distribution of CO sources is fixed inside each of these regions. The inversion scheme optimizes the intensities of the emissions fluxes for the following processes: technological activities, forest and savanna burning, agricultural waste burning and fuelwood use, soil/vegetation emissions, and oceanic emissions. The inversion significantly reduces the uncertainties on the surface sources over Europe, North America and Asia. The most striking result is the increase (almost by a factor of 2) of CO flux from Asia in all a posteriori scenarios. The uncertainties on the Southern Hemisphere emissions remain large after the inversion, because the current observational surface network is too sparse at these latitudes. The inversion, moreover, shifts the peak in biomass burning emissions in the Southern Hemisphere by one month. This temporal shift ensures a better match of the observed and modeled CO seasonal cycle at the Ascension Island station. We also attempted to optimize the annual and global productions of CO due to methane and NMHC. With the current set of data, the scheme was not able to differentiate between these two sources, and hence only the total chemical production of CO can be optimized. *INDEX TERMS:* 0322 Atmospheric Composition and Structure: Constituent sources and sinks; 3210 Mathematical Geophysics: Modeling; 3260 Mathematical Geophysics: Inverse theory; *KEYWORDS:* carbon monoxide, emissions, inverse modeling, CMDL

Citation: Pétron, G., C. Granier, B. Khattatov, J.-F. Lamarque, V. Yudin, J.-F. Müller, and J. Gille, Inverse modeling of carbon monoxide surface emissions using Climate Monitoring and Diagnostics Laboratory network observations, *J. Geophys. Res.*, 107(D24), 4761, doi:10.1029/2001JD001305, 2002.

1. Introduction

[2] It is estimated that the global amount of tropospheric carbon monoxide (CO) has doubled since the pre-industrial

time [Cicerone, 1988; Müller, 1992; Haan *et al.*, 1996], as a result of extensive use of fossil fuel, burning of large zones of forests, and increase in emissions of methane and several other hydrocarbons. In the free troposphere, the primary sink for CO is its oxidation by the major atmospheric “cleansing” agent, the OH radical [Logan *et al.*, 1981]. The global average lifetime of CO is about 2 months [Cicerone, 1988]. An increase in the atmospheric amount of CO could reduce the self-cleansing ability of the atmosphere and thus modify its chemical, physical and climatological properties [Graedel and Crutzen, 1996]. Predicting the full consequences of such an increase is not straightforward, as the distribution of other pollutants could also have an impact on the OH distribution and feedback effects may reduce or amplify the trend. In the presence of sufficiently high nitrogen oxides concentrations and sunlight, CO is a precursor of tropospheric ozone. Therefore, a detailed knowledge of the processes regulating

¹Service d’Aéronomie, Université Paris 6, Paris, France.

²Also at Atmospheric Chemistry Division, National Center for Atmospheric Research, Boulder, Colorado, USA.

³Also at Aeronomy Laboratory, Cooperative Institute for Research in Environmental Sciences-National Oceanic and Atmospheric Administration, Boulder, Colorado, USA.

⁴Also at Max-Planck-Institut für Meteorologie, Hamburg, Germany.

⁵Atmospheric Chemistry Division, National Center for Atmospheric Research, Boulder, Colorado, USA.

⁶Belgian Institute for Space Aeronomy, Brussels, Belgium.

the carbon monoxide distribution is essential in studies of the tropospheric chemistry.

[3] The processes leading to the emission and/or production of CO in the troposphere are fairly well established. Its budget, however, is still uncertain. Its sources and sinks (approximately 90% of the sink being its reaction with OH, the rest being due to dry deposition) are quite variable in space and time. 75% of CO surface sources are located in the Northern Hemisphere. Since the CO lifetime is shorter than the interhemispheric exchange time, the source distribution heterogeneity is reflected in the spatial distribution of the CO mixing ratio at the surface, as measured for example by the NOAA-Climate Monitoring and Diagnostics Laboratory (CMDL) flask sampling network stations [Novelli *et al.*, 1998]. CO mixing ratios at the surface in the Southern Hemisphere are about one third of the surface values measured in the Northern Hemisphere. Manning *et al.* [1997] estimated that, on average, 30% of CO in the Southern Hemisphere extra-tropics is due to Northern Hemisphere sources. Most of the CO sources and sinks also have a high seasonal and interannual variability. Higher mixing ratios of OH in the Northern high latitudes during the summer months significantly increase the CO sink [Novelli *et al.*, 1998]. In the tropics, savanna burning typically occurs at the end of the dry season, the timing of which differs from one region to another [Hao and Liu, 1994; Galanter *et al.*, 2000]. The time and spatial variability of CO sources makes it quite difficult to extrapolate local and noncontinuous measurements of CO fluxes to emissions on the global scale.

[4] Emission inventories are essential inputs to models simulating the composition of the atmosphere and its evolution. Different ranges of global emission fluxes have been proposed by several studies [see, e.g., World Meteorological Organization/United Nations Environment Programme (WMO/UNEP), 1998; Houghton *et al.*, 2001]. CO emissions due to fossil fuel use are estimated to be between 300 and 600 TgCO/yr, biomass burning emissions of CO between 300 and 900 TgCO/yr, vegetation and soil emissions between 50 and 200 TgCO/yr and the oceanic emissions between 6 and 30 TgCO/yr. The production of CO due to the oxidation of methane and nonmethane hydrocarbons (NMHC) ranges between 400 and 1000 TgCO/yr and between 300 and 1000 TgCO/yr respectively. As the ranges given above clearly show, the uncertainties attached to CO global sources are still high. Besides the difficulties mentioned earlier in extrapolating local flux studies (bottom-up approach), accurate estimates of national emissions are available for only few countries. Interannual variations are also not easily predictable as many factors such as change in land use can affect the emissions.

[5] Since CO sources can not be directly monitored on a global scale and regular timescale, scientists have tried to better constrain CO budget using observations of CO mixing ratio together with chemistry-transport models (CTM) of the atmosphere. A monitoring network (CMDL) has been created in the late 1980s to measure the background concentrations of CO (and of other trace gases) at stations located in remote areas. In parallel, chemistry and transport forward models have been developed to reproduce the tropospheric distribution of CO and other chemical compounds using prescribed surface emissions. A forward

CTM is a numerical discrete representation of the relationship between sources and atmospheric mixing ratios. Observed and simulated distributions of atmospheric compounds are compared to improve and validate the models (e.g., chemistry and transport parameterizations) as well as emission inventories. The information contained in the measurements of tropospheric CO distribution together with the information contained in a CTM can also be combined in order to better assess CO sources (top-down approach). This is referred to as inverse modeling.

[6] Inverse techniques aim at optimizing parameters of a system, based on data and knowledge of the theoretical relationship between these data and the parameters. In atmospheric research, inverse techniques have been developed to optimize global emissions of long-lived pollutants using a CTM as a forward model and concentration measurements at surface stations (CFCs by Hartley and Prinn [1993], CO₂ by Enting *et al.* [1995], Bousquet *et al.* [1999a, 1999b], Peylin *et al.* [1999], and Baker [2001], and CH₄ by Hein and Heimann [1994] and Houweling *et al.* [1999]). Manning *et al.* [1997] were the first to develop an inverse model of CO sources. Their scheme optimized 6 annual and global sources using CO mixing ratio and ¹³C data from Baring Head (New Zealand) together with a 2D model. Bergamaschi *et al.* [2000a, 2000b] performed the first 3-D time-independent inversion of eight CO global and annual sources using 31 CMDL stations and the TM2 model [Heimann, 1996]. The present study adopts the time-dependent inverse technique used for the optimization of long-lived tracer sources [Peylin *et al.*, 1999] to optimize monthly CO direct surface emissions for 6 different processes. The spatial distribution of the emission flux for each process is fixed over each of the 7 continental and 5 oceanic regions considered (see Figure 1). This type of inverse modeling is called synthesis inversion as only the average flux intensity over a relatively large region is optimized. This study presents the first inversion of CO sources on a monthly and regional basis. Other techniques have been developed to deduce time-varying sources and sinks. For example, Haas-Laursen *et al.* [1996] and Gilliland and Abbitt [2001] worked on adaptations of the Kalman filter and tested their algorithms with pseudodata. Following this approach, Chang *et al.* [1996, 1997] estimated the hourly emissions of isoprene and CO in Atlanta, Georgia.

[7] Since the late 1980s/early 1990s, CO concentrations have been measured weekly at several stations of the CMDL network. The objective of the present study is to better estimate surface emissions of CO on a monthly timescale, using monthly means of CO mixing ratio observations from the CMDL flask sampling network (<ftp://ftp.cmdl.noaa.gov/ccg/co/flask/README.html>) together with climatological transport inputs in the three-dimensional tropospheric chemistry and transport model IMAGES. Monthly mean CO mixing ratios are obtained from 39 stations of the CMDL network between 1989 and 1996 (Table 1 and Figure 1). These data are compared with the outputs from the IMAGES model described in section 2. The inversion scheme attempts to minimize the discrepancies between observed and modeled mixing ratios at the stations first by optimizing the direct surface emissions of CO alone and then by optimizing the direct surface emissions of CO together with the global chemical production of

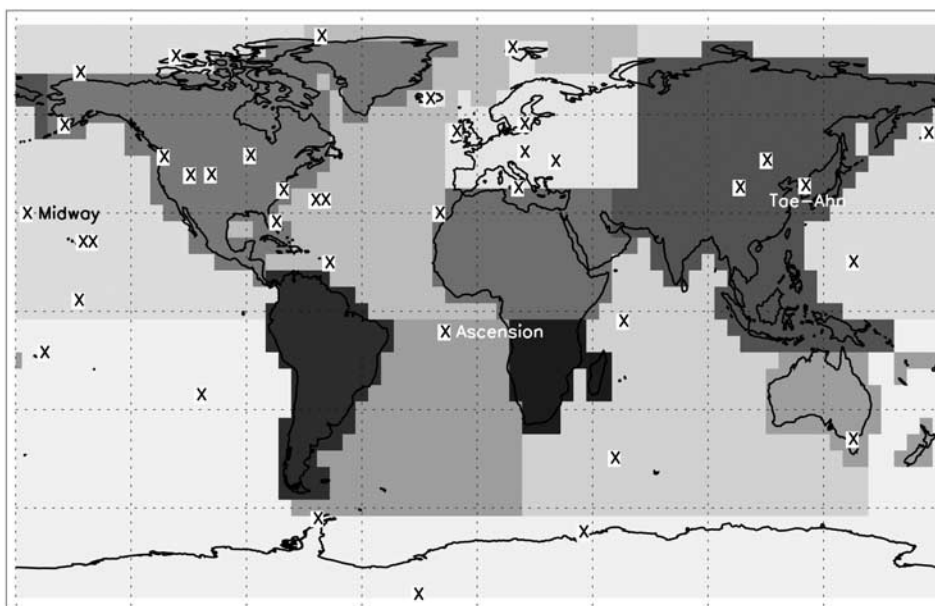


Figure 1. Locations of the 12 emission regions and 39 CMDL stations used in this study.

CO. The direct surface emissions of CO are aggregated over five oceanic and seven continental source regions. The continental surface emissions are subdivided into 4 processes. The geographical distribution of each type of emission is fixed inside each of the source regions and the inverse scheme optimizes the emission intensities for the 12 source regions on a monthly basis.

[8] The inverse technique is presented in section 3, together with a discussion of the observations used in the study, the assumptions and the fundamental numerical equations. Results are shown and discussed in section 4 and, finally, the advantages and limitations of the method will be discussed in section 5.

2. Description of IMAGES

[9] A detailed description of IMAGES (Intermediate Model of the Annual and Global Evolution of Species) is presented by Müller and Brasseur [1995], and the most recent changes are described by Müller and Brasseur [1999] and Granier *et al.* [2000a, 2000b]. Thus, this section only summarizes the major features of the model and gives some recent updates to the surface emissions, the dynamics and the chemistry.

[10] IMAGES has a $5^\circ \times 5^\circ$ horizontal resolution and 25 vertical levels from the surface to 50 hPa, with five levels in the planetary boundary layer and two-three levels in the lower stratosphere. The model transport parameters are specified based on the monthly mean climatological fields from ECMWF (European Centre for Medium-Range Weather Forecasts, <http://www.ecmwf.int/>) analysis (winds, temperature, humidity) for the period 1985–1989. The interannual variability is therefore ignored. IMAGES employs a semi-Lagrangian transport scheme for the tracer advection [Smolarkiewicz and Grell, 1991]. The time-step is one day, except for the first 3 days of each month during which the full diurnal cycle is simulated (0.5 to 1 hour time-

step). Small-scale transport processes are accounted for via macro-scale diffusion coefficients in the zonal and meridional direction. The convection parameterization used is based on Costen *et al.* [1988]. The distribution of cumulonimbus clouds is derived from the International Satellite Cloud Climatology Project (ISCCP), using monthly average data over the period 1984–1987.

[11] The equations controlling the concentrations of O_x , NO_x , HO_x , SO_x compounds and several hydrocarbons and their oxidation products (i.e., key species which are known to have an impact on the tropospheric oxidizing power and on the photochemical production of ozone) are included in IMAGES. The standard chemical scheme of the model includes 43 chemical species (among which 17 compounds are long-lived, i.e., having lifetimes greater than a few hours), 125 chemical reactions and 26 photolytic reactions. The photo-dissociation coefficients are interpolated from pre-calculated tabulated values [Müller and Brasseur, 1995]. ECMWF analyses are used to produce monthly mean distribution of the water vapor mixing ratio. The chemical scheme includes five hydrocarbons (ethane, ethylene, propylene, isoprene, terpenes (α -pinene) and a lumped species that represents the other NMHC chemistry. The same lumping technique is used to reduce the number of intermediate radicals. The oxidation scheme of isoprene is treated with some details based on a scheme proposed by Paulson and Seinfeld [1992].

[12] The model provides estimates of the monthly averaged distribution of several tropospheric chemical species, but it does not reproduce the high frequency variability of some tracer distributions. Therefore, the IMAGES-calculated distributions should only be compared with climatological averages of observed mixing ratio distributions.

[13] The trace gas surface emissions and deposition velocities in the model are monthly mean averages, based on currently available inventories. The emission fields are specified on a $5^\circ \times 5^\circ$ horizontal grid.

Table 1. Longitudes and Latitudes of the 39 NOAA/CMDL In Situ Measurement Stations Used for the Inversion^a

Station	Longitude, decimal degrees	Latitude, decimal degrees
Alert	-62.52	82.45
Ascension Island	-14.42	-7.92
Baltic Sea	16.67	55.50
St. David's Head (Bermuda)	-64.65	32.37
Tudor Hill (Bermuda)	-64.88	32.27
Barrow	-156.60	71.32
Black Sea	28.68	44.17
Cold Bay	-162.72	55.20
Cape Grim	144.68	-40.68
Christmas Island	-157.17	1.70
Cape Meares	-123.97	45.48
Crozet Island	51.85	-46.45
Easter Island	-109.45	-27.15
Guam	144.78	13.43
Dwejra Point	14.18	36.05
Hegyatsal	16.65	46.95
Heimaey	-20.15	63.25
Grifton	-77.38	35.35
Tenerife	-16.48	28.30
Key Biscayne	-80.20	25.67
Cape Kumukahi	-154.82	19.52
Park Falls	-90.27	45.93
Mould Bay	-119.35	76.25
Mace Head	-9.90	53.33
Midway	-177.37	28.22
Mauna Loa	-155.58	19.53
Niwot Ridge	-105.58	40.05
Palmer Station	-64	-64.92
Qinghai Province	100.55	36.16
Ragged Point	-59.43	13.17
Seychelles	55.17	-4.67
Shemya Island	174.10	52.72
Samoa	-170.57	-14.25
South Pole	-24.80	-89.98
Syowa Station	39.58	-69.00
Tac-Ahn	126.13	36.73
Wendover	-113.72	39.90
Ulaan Uul	111.10	44.45
Spitsbergen	11.88	78.90

^a Latitudes north of the equator and longitudes east of the Greenwich meridian are positive (see also the map in Figure 1).

[14] Anthropogenic sources, which include emissions from fossil fuel use (e.g., industry, transportation, fuel production), biofuel combustion, emissions due to specific industrial activities (iron and steel production) and solvent use, waste treatment, and agricultural waste burning, are taken from the EDGAR v2.0 global 1×1 degree inventory developed by *Olivier et al.* [1996]. This inventory provides yearly averages for 1990, and the seasonality is taken from *Müller* [1992], based on the seasonal variation of fossil fuel use and production and on the temperature dependence of vehicle emissions. The technological emissions used in this study correspond to the sum of the fossil fuel, the industrial biofuel and the industrial processes provided by the EDGAR v2.0 database. The agricultural waste burning and fuelwood use source is the sum of the EDGAR v2.0 estimates for the agricultural waste burning source (207.6 TgCO/yr) and the biofuel source (181 TgCO/yr).

[15] The emissions due to forest and savanna fires are taken from *Granier et al.* [2000b]. The monthly averages of the amount of biomass burnt each year in forest and savanna fires are derived from the evaluation by *Hao and Liu* [1994]

at a $5^\circ \times 5^\circ$ horizontal resolution. The conversion to fluxes of non-CO₂ trace gases resulting from these fires is similar to the one described by *Granier et al.* [2000b, Table 2].

[16] Biogenic sources include emissions of NMHC and NO_x by the vegetation and microorganisms in the soil, as well as emission of methane by ruminants, rice paddies, termites and wetlands. Continental biogenic emissions of isoprene, terpenes and other NMHC, and NO_x are taken from the Global Emission Inventory Analysis database (<http://www.geiacenter.org>), based on *Guenther et al.* [1993, 1995]. All other emissions are similar to the ones described by *Müller* [1992]. Global yearly emissions represent 500 TgC/yr for isoprene and 127 TgC/yr for terpenes. The distribution of NO production due to lightning is derived from *Price and Rind* [1994] and *Pickering et al.* [1998]. Dry deposition at the surface accounts for less than 10% of CO global sink. This sink is not optimized in this study. The deposition velocities are fixed and taken from *Müller* [1992, 1993].

[17] The emission of CO by the ocean has a relative distribution derived from *Erickson* [1989] and its total and global flux is close to the middle point of the range recommended by *Brasseur et al.* [1999], based on the study of *Bates et al.* [1995].

[18] The CO anthropogenic emissions used in the model correspond to those for the year 1990. These emissions, together with natural emissions, are taken as the a priori emissions for the inversion scheme. Uncertainties are assigned on the a priori monthly emission fluxes as a percentage of their intensity. Relative uncertainties of 50% are assigned to all surface monthly source flux, except for technological emissions, similar to *Bergamaschi et al.* [2000a]. In this study, everywhere except over Asia, the technological emissions are given a 10% relative uncertainty, reflecting the fact that these emissions are believed to be better known. The Asian technological emissions however are not as much documented, as a result they are given a 50% relative uncertainty.

[19] The “tagging” technique [*Lamarque et al.*, 1996; *Granier et al.*, 2000a], which consists of separating the modeled CO into different tracers depending on its origin (region and type of emission), has been implemented to decrease the number of simulations to be performed.

3. Description of the Inverse Technique

[20] The discrepancies between the observed and the modeled distributions of tropospheric CO can be minimized by optimizing model parameters. In the present study, these parameters are the direct surface emissions of CO. Since we use a climatological CTM, the modeled CO mixing ratios are compared with a long-term measurement program.

3.1. CMDL Measurements of CO

[21] As indicated earlier, this study uses the CMDL measurements of CO mixing ratios at a network of stations, most of which sample marine boundary layer air. There is some evidence that CO surface concentration trends changed significantly at observing sites after the mid-1980s [*Khalil and Rasmussen*, 1994; *Novelli et al.*, 1994]. The observed decrease of CO concentration in the boundary layer was estimated to be 2.6%/yr between 1987 and 1992

by Khalil and Rasmussen [1994] and 2.3%/yr between 1990 and 1995 by Novelli *et al.* [1998]. In 1992 and 1993, observations show a significant decrease in global tropospheric CO [Novelli *et al.*, 1998], part of this change has been related to an increase in OH production resulting from the eruption of Mount Pinatubo in June 1991 [Bekki *et al.*, 1994]. In the Wotawa *et al.* [2001] study of summertime CO concentrations interannual variability in the extra-tropical Northern Hemisphere (ENH, where 22 out of the 39 stations considered in this study are located), the authors pointed out that the ENH CO time series (based on measurements at 17 CMDL stations north of 30°N) from 1991 to 1999 show significant interannual variability but no clear trend. Total columns of CO measured at different sites show either stabilization or a quite small decline during these periods (L. Yurganov, unpublished report, 2000). A steady CO distribution in the atmosphere for the period 1990–1996 is assumed and monthly averages of the measurements are computed (the length of the measurements time series varies by site). These averages are supposed to represent the climatological seasonal cycle of CO distribution during the early 1990s. The interannual variations of CO monthly mean mixing ratios are used to estimate the interannual variability of the CO fields averaged over the period of sampling. The monthly measurement error for each data needs to be provided in the inversion algorithm and is taken to be the maximum of the CO monthly averaged mixing ratio interannual variability at the station and 10% of the data value. This 10% minimal relative uncertainty on the data slightly overestimates the observation errors due to the sampling procedure, the analysis and the data reduction [Novelli *et al.*, 1998], and thus part of these 10% represent the error due to the no-trend hypothesis. 18 out of 39 stations have the interannual variability of their 12 monthly mean CO mixing ratios below 10%. The interannual variabilities of the 12 monthly mean CO mixing ratios are below 20% at 17 other stations. Finally for 4 stations (Black Sea, Hegyhatsal, Dwejra Point and Tae-Ahn), the interannual variability of monthly mean CO mixing ratios reaches a value over 20% for at least one month. The synoptic variability within a month is not taken into account as the CTM uses monthly averaged wind fields and cannot consequently reproduce high frequency events. The observation error is the minimal estimate of the uncertainty on the data at the stations since the modeling error (also called the representation error) is not added [see Tarantola and Valette, 1982a, section 10]. Some results are described in Appendix B, which show the impact of adding the modeling errors to the measurement errors in the inversion scheme. 30 of the CMDL stations are located in the Northern Hemisphere. There are no stations in Africa and South America. The CMDL measurements correspond to clean air conditions at local stations. For stations near the coast (Cape Grim, Key Biscayne, Mace Head) only air originating from the marine boundary layer is sampled. The model provides mixing ratios averaged over a grid box of 5° × 5°, and no filtering is applied for wind directions.

3.2. Numerical Method

[22] In this synthesis inversion study, four types of emissions for 7 continents (emissions due to technological activities, biomass burning (2 subcategories: (1) forest and

savanna burning and (2) agricultural waste burning and fuelwood use) and vegetation/microorganisms in soils) and 5 oceanic source regions bring a total of 33 tagged CO sources, $\tilde{\mathbf{x}}$. At first, only the direct surface emissions of CO are optimized, as specified earlier. The emissions of CO precursors (methane and NMHC) are fixed, except in the last inversion study. The amount of CO chemically produced from the oxidation of hydrocarbons is derived from the chemistry-transport model itself.

[23] The relationship between the vector of $N_x = 12 \times 33$ monthly CO surface fluxes $\mathbf{x} = (x_i)_{i=1, N_x} = (\tilde{\mathbf{x}}_{\text{january}}, \tilde{\mathbf{x}}_{\text{february}}, \dots, \tilde{\mathbf{x}}_{\text{december}})$ and the vector of $N_y = 12 \times 39$ monthly mean CO mixing ratios at the stations $\mathbf{y} = (y_j)_{j=1, N_y} = (\tilde{\mathbf{y}}_{\text{january}}, \tilde{\mathbf{y}}_{\text{february}}, \dots, \tilde{\mathbf{y}}_{\text{december}})$ can be written as $\mathbf{y} = \mathbf{H}(\mathbf{x})$. We assume that a linear approximation can be used locally, i.e., in the vicinity of a reference state of the system characterized by the a priori emissions \mathbf{x}^b . It will be shown later (section 4.4) that the linearization assumption holds sufficiently well for the tropospheric CO chemistry. The linearized relationship between $(\mathbf{x}_i)_{i=1, N_x}$ and $(\mathbf{y}_j)_{j=1, N_y}$ around \mathbf{x}^b can be represented by a matrix $\mathbf{H}(N_y, N_x)$. This matrix is calculated by simulating the impact of each CO surface monthly flux (for example, technological emissions of CO over the Northern American continent in August) on the CO monthly mean mixing ratios at the stations. For these simulations, the chemical state of the atmosphere (OH concentrations) is the same as the one computed by the full chemistry model using the a priori emissions. \mathbf{H} is later referred to as the observation matrix (see Figure 3 from Peylin *et al.* [1999] for a schematic representation of the \mathbf{H} matrix for a time-dependent inversion problem).

[24] As the calculations of the observation matrix coefficients require a very large amount of computer time, the construction of \mathbf{H} has been made possible by simplifying the model to a reasonable extent. Hence, a tracer version of the IMAGES model has been written. It uses monthly OH distributions computed off-line by running the full version of the CTM. The tracer version of IMAGES reads the 33 tagged CO surface fluxes each month and contains 33 CO tracers reacting with the fixed OH. The agreement on the CO distribution between the full model and the tracer version for CO is good to within a few percent, as far as CO emitted at the surface is concerned. Nevertheless, the computational cost stays quite significant and limits our ability to perform numerical experiments.

[25] To calculate the impacts at the stations of month m fluxes, the CO-tracer model is run for 6 months with fixed OH monthly 3-D distributions, and starting at the beginning of month m with an atmosphere free of CO. All fluxes are set to zero, except for the first month of simulation. The model therefore computes the lasting impact on CO distribution of each of the 33 tagged CO surface fluxes emitted during month m . The simulated monthly averaged mixing ratios for the 33 tagged CO tracers are saved at the stations location. To get the \mathbf{H} matrix coefficients, these values are divided by the respective intensity of the tagged fluxes of month m . Let $\mathbf{H}_{m \Rightarrow n}$ be the matrix of dimension 39×33 representing the normalized impact of month m fluxes on month n observations. A block-representation of the \mathbf{H} matrix (equivalent to the one of Peylin *et al.* [1999], with a few permutations of lines) is given in Figure 2. The impact of any monthly flux has been truncated to only last 6 months. This assumption

Stations/Sources		monthly 33 tagged fluxes											
		Jan	Feb	Mar	Apr	May	Jun	Jul	Aug	Sep	Oct	Nov	Dec
normalized contributions to monthly [CO] at the 39 stations ppbv/TgCO	Jan	$H_{1 \Rightarrow 1}$	0	0	0	0	0	0	$H_{8 \Rightarrow 1}$	$H_{9 \Rightarrow 1}$	$H_{10 \Rightarrow 1}$	$H_{11 \Rightarrow 1}$	$H_{12 \Rightarrow 1}$
	Feb	$H_{1 \Rightarrow 2}$	$H_{2 \Rightarrow 2}$	0	0	0	0	0	0	$H_{9 \Rightarrow 2}$	$H_{10 \Rightarrow 2}$	$H_{11 \Rightarrow 2}$	$H_{12 \Rightarrow 2}$
	...	$H_{1 \Rightarrow 3}$	$H_{2 \Rightarrow 3}$	$H_{3 \Rightarrow 3}$	0	0	0	0	0	0	$H_{10 \Rightarrow 3}$	$H_{11 \Rightarrow 3}$	$H_{12 \Rightarrow 3}$
	...	$H_{1 \Rightarrow 4}$	$H_{2 \Rightarrow 4}$	$H_{3 \Rightarrow 4}$	$H_{4 \Rightarrow 4}$	0	0	0	0	0	0	$H_{11 \Rightarrow 4}$	$H_{12 \Rightarrow 4}$
	...	$H_{1 \Rightarrow 5}$	$H_{2 \Rightarrow 5}$	$H_{3 \Rightarrow 5}$	$H_{4 \Rightarrow 5}$	$H_{5 \Rightarrow 5}$	0	0	0	0	0	0	$H_{12 \Rightarrow 5}$
	...	$H_{1 \Rightarrow 6}$	$H_{2 \Rightarrow 6}$	$H_{3 \Rightarrow 6}$	$H_{4 \Rightarrow 6}$	$H_{5 \Rightarrow 6}$	$H_{6 \Rightarrow 6}$	0	0	0	0	0	0
	...	0	$H_{2 \Rightarrow 7}$	$H_{3 \Rightarrow 7}$	$H_{4 \Rightarrow 7}$	$H_{5 \Rightarrow 7}$	$H_{6 \Rightarrow 7}$	$H_{7 \Rightarrow 7}$	0	0	0	0	0
	...	0	0	$H_{3 \Rightarrow 8}$	$H_{4 \Rightarrow 8}$	$H_{5 \Rightarrow 8}$	$H_{6 \Rightarrow 8}$	$H_{7 \Rightarrow 8}$	$H_{8 \Rightarrow 8}$	0	0	0	0
	...	0	0	0	$H_{4 \Rightarrow 9}$	$H_{5 \Rightarrow 9}$	$H_{6 \Rightarrow 9}$	$H_{7 \Rightarrow 9}$	$H_{8 \Rightarrow 9}$	$H_{9 \Rightarrow 9}$	0	0	0
	...	0	0	0	0	$H_{5 \Rightarrow 10}$	$H_{6 \Rightarrow 10}$	$H_{7 \Rightarrow 10}$	$H_{8 \Rightarrow 10}$	$H_{9 \Rightarrow 10}$	$H_{10 \Rightarrow 10}$	0	0
	...	0	0	0	0	0	$H_{6 \Rightarrow 11}$	$H_{7 \Rightarrow 11}$	$H_{8 \Rightarrow 11}$	$H_{9 \Rightarrow 11}$	$H_{10 \Rightarrow 11}$	$H_{11 \Rightarrow 11}$	0
	Dec	0	0	0	0	0	0	$H_{7 \Rightarrow 12}$	$H_{8 \Rightarrow 12}$	$H_{9 \Rightarrow 12}$	$H_{10 \Rightarrow 12}$	$H_{11 \Rightarrow 12}$	$H_{12 \Rightarrow 12}$

Figure 2. Schematic representation of the observation matrix \mathbf{H} (the submatrix $H_{1 \Rightarrow 2}$ represents the normalized impact of the January emissions on the CO mixing ratios in February at the stations locations, as computed by the model). Each $H_{n \Rightarrow m}$ matrix has the dimension (39, 33). We note $H_{\Rightarrow m} = (H_{1 \Rightarrow m}, H_{2 \Rightarrow m}, \dots, H_{12 \Rightarrow m})$, the m th row in the representation above.

allowed us to divide by a factor of 2 the computer time needed to build \mathbf{H} and it contributes, to some extent, to a better conditioning of \mathbf{H} by replacing small coefficients with zeroes. This assumption is justified when considering the following results.

[26] First the singular values of 6 subspaces of the \mathbf{H} matrix ($\mathbf{H}_{m \Rightarrow \text{June}})_{m = \text{January, June}}$ have been computed and plotted (Figure 3). The singular values of $\mathbf{H}_{\text{April} \Rightarrow \text{June}}$ (reflecting the capacity of June observations to constrain April emissions) are smaller than the corresponding singular

values of $\mathbf{H}_{\text{June} \Rightarrow \text{June}}$. For emissions older than two months ($m = \text{January to April}$), the SVD spectrum drops quite rapidly. It means that only a few fluxes are still well constrained by the June observations. The shape and range of the 6 SVD spectra are quite similar. The SVD plot would be quite similar if we were considering December observations (or any other month) and the emissions of the previous 6 months. From this analysis, we infer that six months after CO was emitted, the observations at the stations contain little information about the emissions.

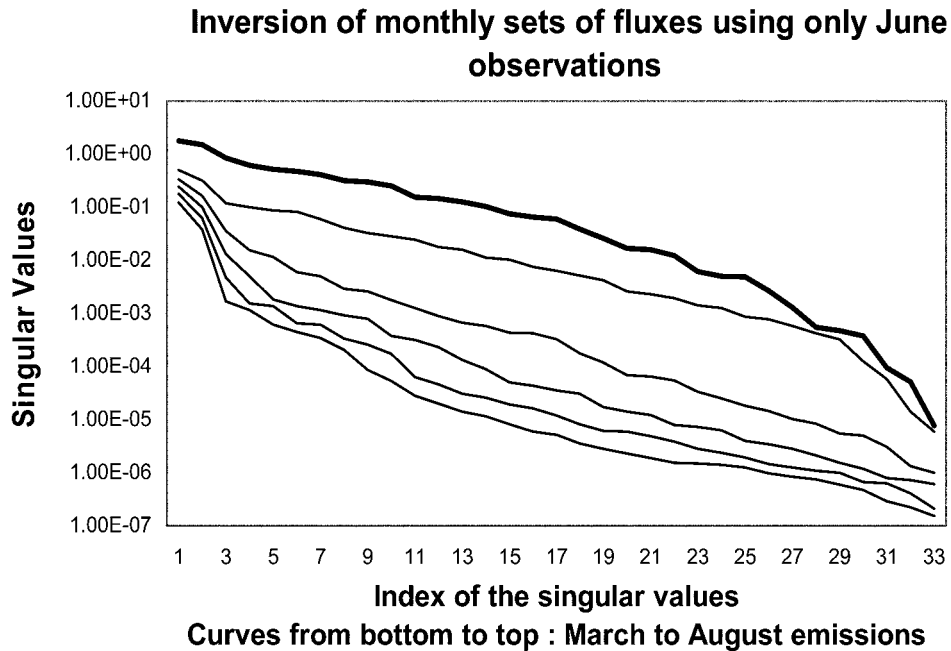


Figure 3. Singular value spectra of the 6 submatrices ($H_{m \Rightarrow \text{June}})_{m = \text{January, June}}$ (each submatrix has the dimension 39*33) The bold line shows the SVD spectrum of the $H_{\text{June} \Rightarrow \text{June}}$ matrix, which gives the modeled impact of June emissions on June CO mixing ratios at the stations. The subsequent lower lines show the SVD spectra of the submatrices giving the impacts of January emissions (bottom line), February emissions (second line),...and, finally, May emissions (line right below the bold line).

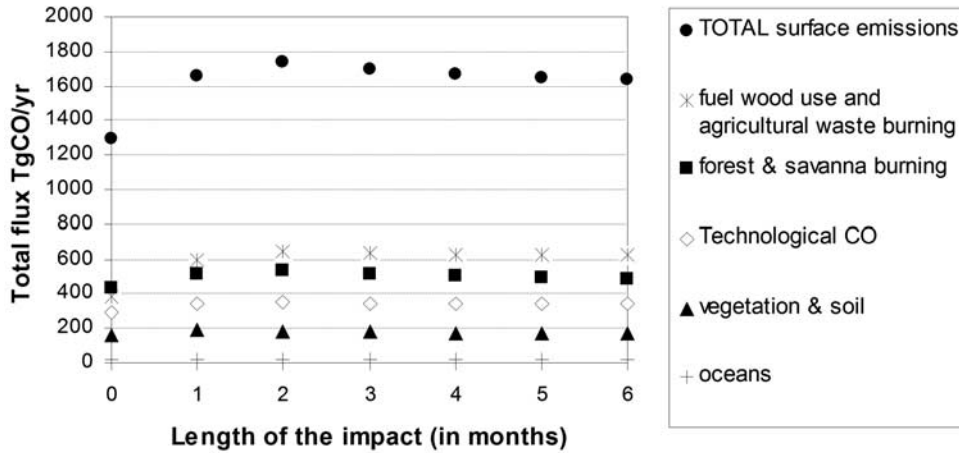


Figure 4. Evolution of the analysis when the impact of monthly emissions is set to last one to six months in the observation matrix \mathbf{H} . Values on the vertical axis are the a priori global estimates for 6 surface sources.

[27] Six preliminary inversions were performed to further test the assumed six-month-long contribution of the surface CO monthly emissions to the stations CO mixing ratios. For these inversions, the impact timescale was set to last up to 6 months. For the first inversion, observations of month m were assumed to depend only on the emissions from month m . Figure 4 shows the evolution of the a posteriori global and annual flux for each process, depending on how long the impact timescale of all monthly emissions was assumed to last. The values corresponding to “zero”-month-long impact are the a priori intensities. As can be seen on the plot, for an impact lasting from 3 to 6 months (last four inversions), the a posteriori yearly fluxes hardly change. For each region and each process, the yearly emissions vary by less than 6% around a mean value in these four inversions, except for the forest and savanna burning source over Southern America (15%). Completing an inversion with a 3-month-long impact for all CO surface monthly fluxes, the a posteriori fluxes have a seasonal cycle and monthly intensities within a 0 to 10% relative difference compared to the “standard” inversion results (assuming a six-month-long impact). Moreover, the a posteriori uncertainties on the fluxes are not affected. These results validate our choice to limit the impact timescale of the monthly emissions on the stations CO mixing ratios to 6 months.

[28] Given the dimensions of the vector of 396 monthly mean fluxes, \mathbf{x} , and the dimension of the vector of 468 monthly mean observations at the stations, \mathbf{y} , the problem appears to be over-determined. In general, since there are more equations than unknowns and given errors in the observations, there is no solution $(x_i)_{i=1, N_x}$ that exactly satisfies the N_y equations $\mathbf{y} = \mathbf{h}(\mathbf{x})$. To solve such problem, a common technique is to look for the best solution in the least squares sense [Lanczos, 1961] and thus to minimize the quadratic sum of the differences between the two sides of the equation: $J(\mathbf{x}) = (\mathbf{h}(\mathbf{x}) - \mathbf{y})^T (\mathbf{h}(\mathbf{x}) - \mathbf{y})$. In this equation, the errors on the observations are not represented and the L2 norm is considered, giving the same weight to each observation.

[29] For reasons discussed in Appendix A, the solution obtained by minimizing J is often not unique and the problem is said to be ill constrained. When the “true” solution of the problem is known to be confined in some domain (for example, Gaussian distribution around a best a priori estimate \mathbf{x}^b) and the errors in the observations, ϵ , are also known, the problem is well constrained and it has a unique solution. However, this solution will now depend on the a priori information used and on the degree of confidence put on it.

[30] Most geophysical inverse studies use the concept of conjunction of independent states of information. They aim at making the best use of the a priori knowledge of a system and of the information contained in data to better estimate poorly known parameters of the system [Tarantola and Valette, 1982a, 1982b; Tarantola, 1987]. To assign weights to these two types of information, a precise description of their uncertainties/errors is necessary. Basically, the a posteriori value of a parameter will be constrained the most by the most reliable piece of information. With the assumptions that the system is linear around its a priori state and that all errors are independent and Gaussian, the least squares criterion becomes equivalent to the maximum likelihood estimator. The best solution of the system, $\mathbf{y} = \mathbf{h}(\mathbf{x}^b) + \mathbf{H}(\mathbf{x} - \mathbf{x}^b) + \epsilon$, now in the weighted least squares sense, is the set of parameters which minimizes the weighted sum of the quadratic distance between the CO mixing ratios observed at the stations and the corresponding model outputs and the quadratic distance between the a priori and the new sets of parameters.

[31] With the notations described below, the best solution of the system can be obtained by minimizing the following function with respect to \mathbf{x} :

$$J(\mathbf{x}) = (\mathbf{h}(\mathbf{x}) - \mathbf{y})^T \mathbf{R}^{-1} (\mathbf{h}(\mathbf{x}) - \mathbf{y}) + (\mathbf{x} - \mathbf{x}^b)^T \mathbf{P}_b^{-1} (\mathbf{x} - \mathbf{x}^b)$$

[32] With the assumptions above, the solution can be fairly well approached (with the hypothesis of weak non-

Table 2. Regional Surface Emission Fluxes of CO Due to Different Processes^a

Type of Emission	Technological			Forest and Savanna Burning			Agricultural Waste Burning and Fuelwood Use			Soil and Vegetation			Total With Global Oceanic Source, TgCO/yr		
	A	First Inversion Analysis	Second Iteration Analysis	A	First Inversion Analysis	Second Iteration Analysis	A	First Inversion Analysis	Second Iteration Analysis	A	First Inversion Analysis	Second Iteration Analysis	A	First Inversion Analysis	Second Iteration Analysis
Europe	97.9	99.8	95.9	10.1	11.2	10.1	43.8	53.4	43.4	10.8	11.4	10.7	162.6	175.8	160.1
Asia	78.4	124.1	120.4	71.8	110.1	90.2	205.1	421.0	428.7	39.9	53.1	46.7	395.2	708.3	686
Northern Africa	14.0	14.0	14.1	103.7	122.3	125.8	56.1	64.5	71.3	23.6	24.4	23.5	197.4	225.2	234.7
Southern Africa	3.8	3.8	3.8	61.7	57.4	66.2	16.8	15.4	13.4	16.1	15.5	17.1	98.4	92.1	100.5
Oceania	3.6	3.6	3.6	17.6	17.0	17.9	2.2	1.6	2.2	7.6	5.5	7.3	31	27.7	31.0
Northern America	82.4	83.9	82.1	54.4	59.7	51.1	37.2	46.1	45.3	18.7	21.2	18.8	192.7	210.9	197.3
Southern America	13.5	13.4	13.4	117.6	108.3	98.8	22.7	19.8	21.2	48.4	41.9	37.9	202.2	183.4	171.3
Total TgCO/yr	293.6	342.6	333.3	436.9	486	460.1	383.9	621.8	625.5	165.1	173	162	1295.9	1639.9	1597.3

^a Surface emission fluxes are given in TgCO/yr. Each process section is divided into three subcolumns that show the intensities of (1) the a priori sources (first column), (2) the a posteriori sources computed in the first inversion (second column), and (3) the a posteriori sources when the inversion was iterated a second time (third column).

linearity) by minimizing:

$$J'(\mathbf{x}) \approx (\mathbf{h}(\mathbf{x}^b) + \mathbf{H}(\mathbf{x} - \mathbf{x}^b) - \mathbf{y})^T \mathbf{R}^{-1} (\mathbf{h}(\mathbf{x}^b) + \mathbf{H}(\mathbf{x} - \mathbf{x}^b) - \mathbf{y}) + (\mathbf{x} - \mathbf{x}^b)^T \mathbf{P}_b^{-1} (\mathbf{x} - \mathbf{x}^b)$$

$$J'(\mathbf{x}) \approx \alpha + 2(\mathbf{x} - \mathbf{x}^b)^T \mathbf{H}^T \mathbf{R}^{-1} (\mathbf{h}(\mathbf{x}^b) - \mathbf{y}) + (\mathbf{x} - \mathbf{x}^b)^T [\mathbf{H}^T \mathbf{R}^{-1} \mathbf{H} + \mathbf{P}_b^{-1}] (\mathbf{x} - \mathbf{x}^b)$$

where α is a constant.

[33] The minimization of J' provides the solution, called the a posteriori sources \mathbf{x}^a , by combining the information contained in the following entities: (1) The first one is the a priori set of monthly surface fluxes \mathbf{x}^b , of dimension $N_x = 33 \times 12 = 396$. Theoretically, \mathbf{x}^b is taken to be the mean for the set of real (“true”) surface fluxes intensities \mathbf{x}_{true} for the true distribution of CO, \mathbf{y}_{true} . The fluxes are expressed in TgCO/yr. The CO surface annual fluxes used as a priori in this study are given in the first column of Table 2. (2) The second one is the vector of observations \mathbf{y} , of dimension $N_y = 39 \times 12 = 468$. Theoretically, \mathbf{y} is taken to be the mean for the set of real (“true”) observations \mathbf{y}_{true} , expressed in ppbv. (3) The third one is the observation matrix \mathbf{H} (N_y, N_x). It represents the monthly averaged contributions at all stations and over 6 months of each monthly tagged CO surface flux normalized to 1 TgCO/yr (around the a priori state). This way, the vector $\mathbf{h}(\mathbf{x}^b) + \mathbf{H}(\mathbf{x} - \mathbf{x}^b)$ gives the total modeled mixing ratios of CO at the stations in ppbv, \mathbf{x} being the CO emissions close to \mathbf{x}^b . (4) The fourth and fifth entities are the covariance matrices \mathbf{P}_b (N_x, N_x) of \mathbf{x}^b and \mathbf{R} (N_y, N_y) of observations \mathbf{y} . The vector of observation errors ϵ ($\mathbf{y} = \mathbf{y}_{\text{true}} + \epsilon$) and the vector of a priori errors on the emissions ξ ($\mathbf{x}_{\text{true}} = \mathbf{x}^b + \xi$) are assumed to have a zero mean. This is equivalent to supposing there is no bias in either the observations or the emissions estimates. Moreover, since the errors are supposed to be independent, \mathbf{P}_b and \mathbf{R} are diagonal matrices and the diagonal terms are the variances of the a priori emissions errors $(\xi_i)_{i=1, N_x}$ and of the observation errors $(\epsilon_j)_{j=1, N_y}$, respectively.

[34] The solution of the minimization problem is called the a posteriori set of surface fluxes or the analysis \mathbf{x}^a . Here, it is easy to derive the expression of the solution analytically from deriving J' with respect to \mathbf{x} . The equations for the a posteriori sources vector \mathbf{x}^a and its corresponding a posteriori covariance matrix \mathbf{P}^a are given below [Gelb, 1974; Tarantola, 1987; Talagrand, 1997]:

$$\mathbf{x}^a = \mathbf{x}^b + [\mathbf{H}^T \mathbf{R}^{-1} \mathbf{H} + \mathbf{P}_b^{-1}]^{-1} \mathbf{H}^T \mathbf{R}^{-1} (\mathbf{y} - \mathbf{h}(\mathbf{x}^b)) \quad (1)$$

$$\mathbf{P}^a = [\mathbf{H}^T \mathbf{R}^{-1} \mathbf{H} + \mathbf{P}_b^{-1}]^{-1}$$

Tarantola [1987] shows that these equations are equivalent to the following ones:

$$\mathbf{x}^a = \mathbf{x}^b + \mathbf{P}_b \mathbf{H}^T [\mathbf{H} \mathbf{P}_b \mathbf{H}^T + \mathbf{R}]^{-1} (\mathbf{y} - \mathbf{h}(\mathbf{x}^b)) \quad (2)$$

$$\mathbf{P}^a = \mathbf{P}_b - \mathbf{P}_b \mathbf{H}^T [\mathbf{H} \mathbf{P}_b \mathbf{H}^T + \mathbf{R}]^{-1} \mathbf{H} \mathbf{P}_b$$

[35] *Haas-Laurson et al.* [1996] used equation (2) to solve for time-varying emissions using pseudo observations and various adaptations of the Kalman filter. By using the same notations, we can show that the solution of the minimization problem takes the same form in both studies (equations (1) or (2)), however the two approaches use different state vectors and representations for the observation matrix. In the paper by *Haas-Laurson et al.* [1996], the observation matrix at time step m was the Jacobian matrix of the change in the concentrations at observing sites at time step m , $\mathbf{Y}(m)$, due to a change in the sources during this specific time step m only, $\mathbf{X}(m)$. In the paper by *Haas-Laurson et al.* [1996], the analysis for time step m (emissions + covariance matrix) was used as prior for time step $m + 1$. In our study, the submatrix $H_{\rightarrow m}$ of the observation matrix \mathbf{H} (see Figure 2) represents the contributions of the emissions from the previous 6 months, $\mathbf{x}(m) = (\mathbf{X}(m), \mathbf{X}(m - 1), \mathbf{X}(m - 2), \mathbf{X}(m - 3), \mathbf{X}(m - 4), \mathbf{X}(m - 5))$, to the average concentrations at the CMDL stations for month m . The subsets of monthly emissions, $\mathbf{X}(m)_{m=1,12}$, and their variances are independent from each other. The adjustment of the emissions of previous months $m^- \leq m$ is used to solve for the residuals of month m . The inversion is not repeated for each monthly set of observations. It is performed “globally” for all observations (or residuals) and all emissions in one single computation. Comparing results obtained with different adaptations of the Kaman Filter, *Haas-Laurson et al.* [1996] concluded that the most accurate method to retrieve the “correct” emissions is the adaptive-iterative Kalman filter. In our study, the inversion is only iterated once to test the nonlinearity of our problem. Fairly good results were obtained after the first inversion, as discussed at the end of this section.

[36] The combination of measurements, a priori and theoretical information allows us to deduce the a posteriori state of information for the emissions. This state is optimal for the assumed statistics when the problem is linear. The nonlinear chemistry of CO-OH does not significantly violate this assumption. The tracer model is a linearized formulation, which approximates quite well the behavior of the full model for sources not too different from the a priori ones.

[37] The emission fields used as prior in the model fix the geographical location of the sources, which is assumed to be climatologically correct. This assumption is more questionable for highly variable sources such as emissions due to biomass burning. The synthesis inversion technique does not optimize for the location of the emissions of CO inside the large regions tagged (see Figure 1). It uses the fixed spatial distribution of the a priori emissions on the model surface grid and optimizes the total intensity of CO fluxes over the 12 regions.

[38] The quality of the inverse method presented above was first tested using pseudodata. The pseudo data set has been created by running the full model with prescribed “true” sources and by archiving the simulated monthly mean CO mixing ratios at the CMDL station locations. For the inversion, 0% to 20% random relative errors have been added (1) to the pseudodata (modeled CO mixing ratios at the stations) to create pseudo observations and (2) to the “true” sources to create a first (nonoptimal) guess or prior for the sources. This test attempts to reproduce the

“real” problem of the atmospheric tracer sources inversion; that is, nothing is known perfectly. In the inversion scheme, the relative errors on the pseudo observations and on the a priori sources have been set to 20%. Ten inversions have been performed. Each inversion has used one vector of pseudo observations and one vector of a priori emissions, none of these being the “truth.” Given the reasonable amplitude of the perturbation applied to the “true” sources and the “true” observations, the inverse scheme had to be able to retrieve a fairly close estimate of the “true” sources to be qualified for the rest of the study. The 10 sets of a posteriori surface sources were compared to the “true” sources. On the yearly basis, the maximum relative mean deviation of the a posteriori emissions from the “true” emissions is 4.7%, occurring for European CO emissions due to agricultural waste burning and fuelwood use. The seasonal cycles for forest and savanna burning emissions, soils and vegetation emissions and oceanic emissions are properly retrieved, even though on the monthly basis, the random errors added to the pseudodata introduce some small dispersion of the a posteriori emissions around the “true” sources. This point underlines the consistency expected by the inversion scheme between the seasonality of the emissions and the seasonality of the observed CO mixing ratios at the stations. One inversion was however sufficient to get a reasonably good estimate of the monthly emissions used to create the pseudodata.

4. Results and Discussion

4.1. Results of the Inversions

[39] Carbon monoxide monthly surface sources are optimized assuming a six-month-long impact timescale at the stations and using a synthesis inversion technique (see assumptions in section 3.2). Yearly averaged regional a posteriori fluxes are presented in Table 2, columns in the middle, and the regional and seasonal source distributions for the three major continental processes (emissions due to technological activities and to biomass burning) are shown in Figure 5. Plots of CO monthly mean mixing ratios at 6 CMDL stations are given in Figure 6. The different lines correspond to the observations (black circles), the observations plus/minus the square root of the observed variability (two bold lines, no symbols), the simulated mixing ratios obtained with the a priori (diamonds) and the a posteriori emissions (squares).

[40] The yearly global surface emission flux of CO increases from the a priori 1295.5 TgCO/yr up to 1639.5 TgCO/yr. This increase is mostly due to the new estimate for the annual flux over Asia: 708.3 TgCO/yr in comparison with the 355.3 TgCO/yr for the prior. Total emissions over Europe and Northern America are increased by less than 10%.

[41] As pointed out by *Holloway et al.* [2000], the technological emission taken from EDGAR-v2 is underestimated, especially for Asia. The a posteriori global technological emission obtained here is 342.6 TgCO/yr, to be compared with its a priori value of 293.6 TgCO/yr (slightly less than the 297 TgCO/yr of the original inventory due to the mapping of the sources in the tracer model). The new seasonality of the global technological source is mostly due to a seasonality change of the emissions over Asia. As

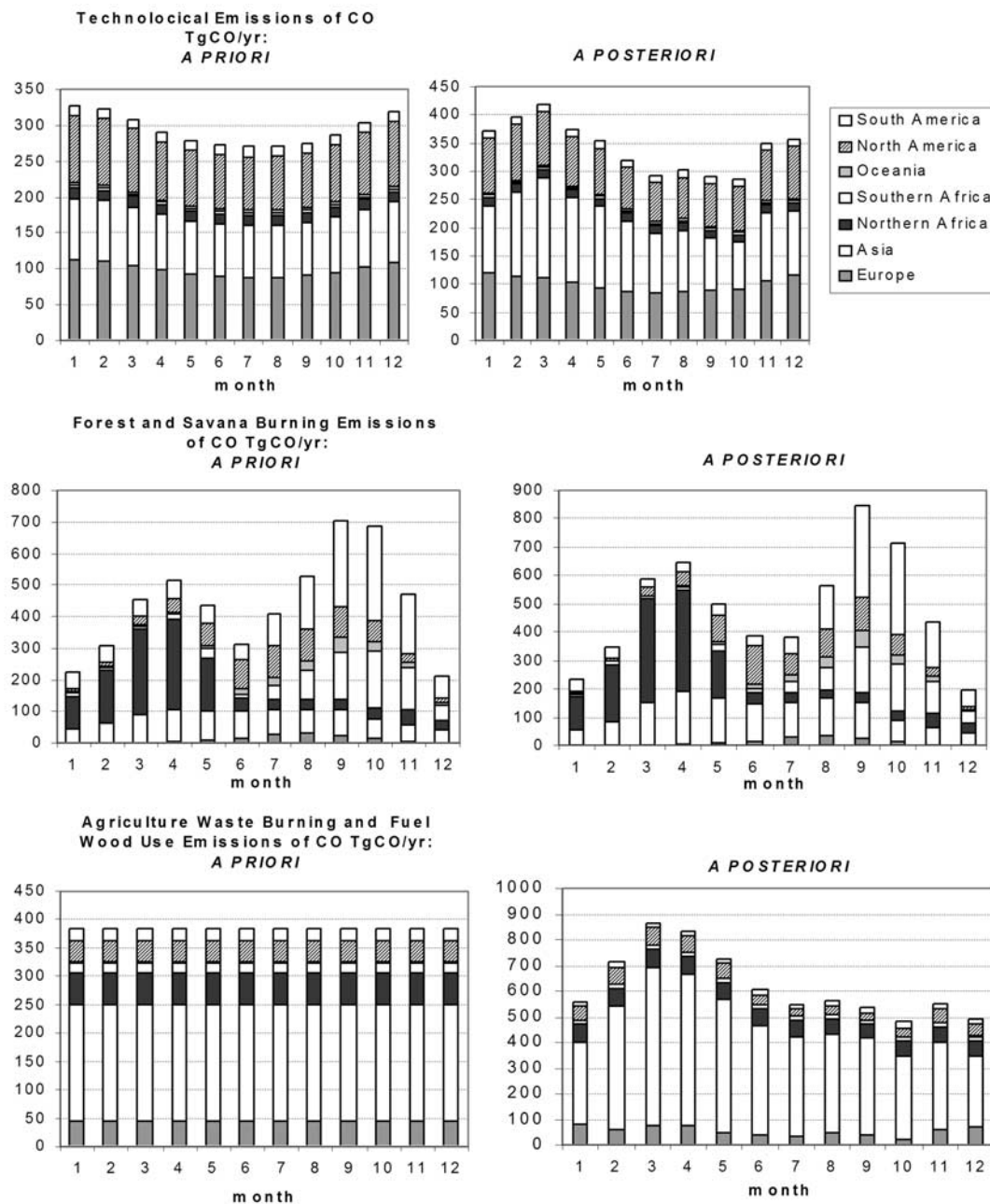


Figure 5. Seasonal distribution of CO technological and biomass burning sources. In each column, the different patterns show the contributions due to the 7 continental regions considered in the synthesis inversion. The plots on the left correspond to the a priori emissions, and the plots on the right to the a posteriori emissions.

explained in the next paragraphs, this new seasonality is probably an artifact of the method.

[42] The biggest changes from the a priori values occur in Asia, where the a priori uncertainties on the emissions are quite high. For the Asian region, the a posteriori CO surface emissions due to industrial activities and forest burning are increased by 58% and 53% respectively. The most striking feature over Asia though is the large increase in the emission flux due to agricultural waste burning and fuel-wood use. The intensity of this flux doubles on an annual basis compared to the a priori values we used; it even triples

in March, reaching a peak over 600TgCO/yr. These results point out that the already high uncertainties in the Asian sources may have been underestimated since the deviation of the solution from the a priori values was assumed to be within a 50% range. Furthermore, because the technological source and the two types of biomass burning emissions over Asia have similar seasonal impacts, in the model, at the downwind stations, these three sources cannot be distinguished in the inverse modeling approach. The differences between these sources' spatial distributions over Asia are not seen by the network. As a result, the inversion modifies

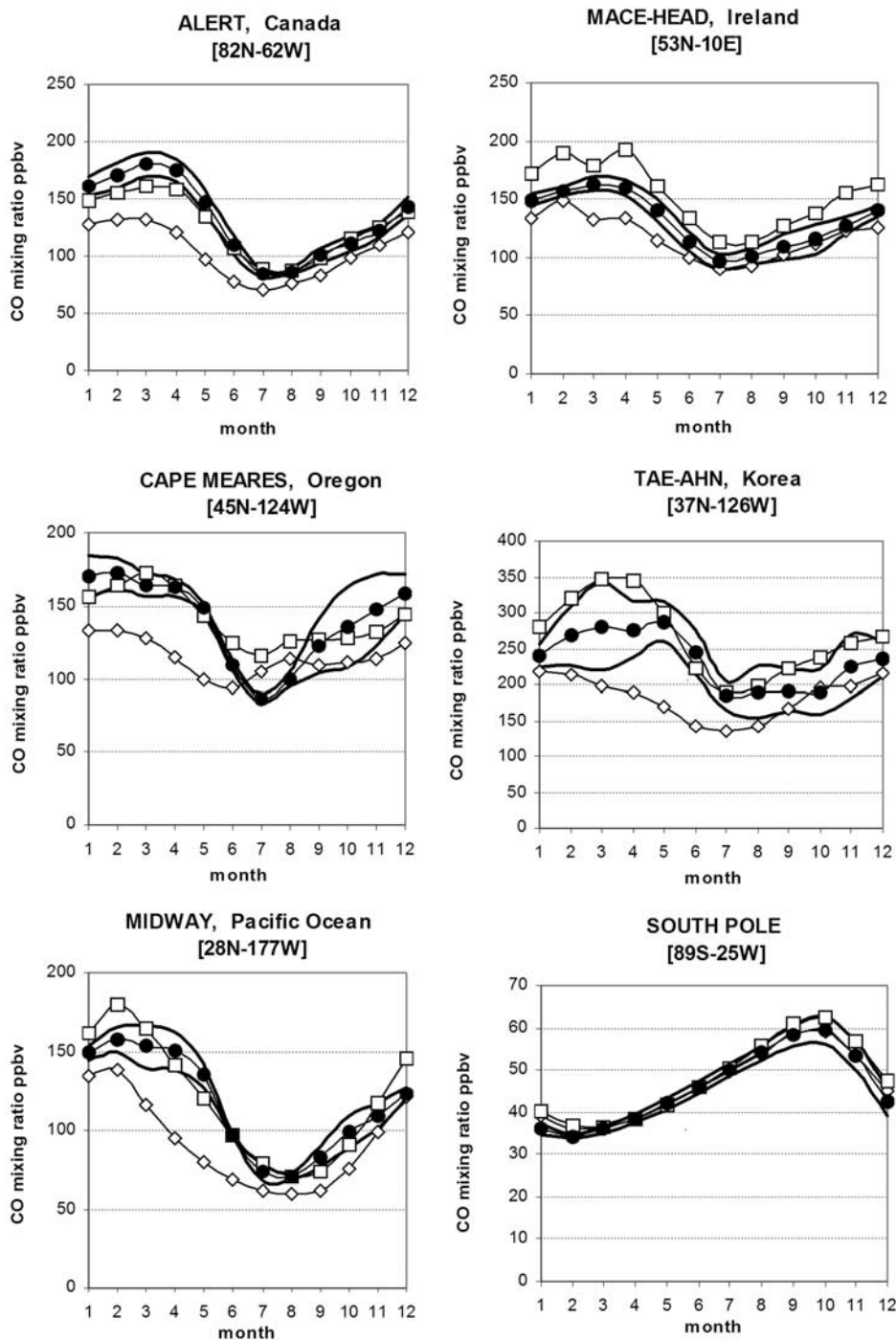


Figure 6. Observed and simulated CO mixing ratios (ppbv) at 6 CMDL stations. The black dots correspond to the observations. The bold lines with no symbol show the standard deviation of the observations. The open diamonds correspond to CO simulated using the a priori emissions, and the open squares correspond to CO simulated using the a posteriori emissions.

these 3 fluxes into similar seasonal patterns. As a sensitivity test, a second inversion is performed, where the 3 sources are aggregated into one single source having an assumed 100% mean deviation. The new a posteriori seasonal cycle for the Asian aggregated source has the same shape as the one from the previous inversion. It peaks in March at almost 1200 TgCO/yr. The annual flux over Asia is 743.5 TgCO/yr.

The emissions over Europe and the Northern American continent are 168.9 and 197 TgCO/yr. In the previous analysis, these fluxes were 175.8 and 210.9 TgCO/yr.

[43] In order to understand the increased peak of the March Asian flux, the assumptions made for the previous inversion are used (same a priori emissions and diagonal covariance matrices). For this experiment, the technological

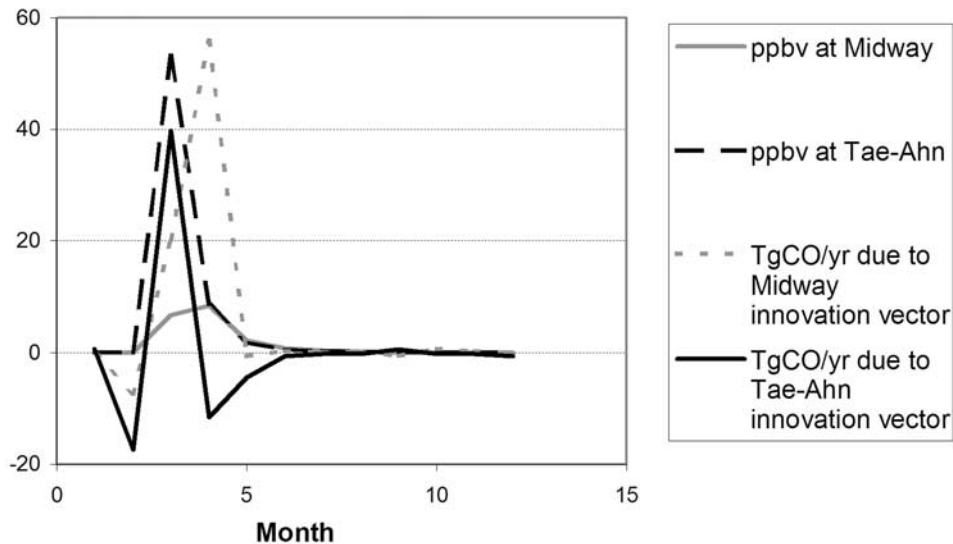


Figure 7. Origin of the March Asian increased peak. The first two curves show the modeled contributions in ppbv of the March aggregated Asian source to the concentrations at Midway and Tae-Ahn over a year. The last two curves show the contributions in TgCO/yr of the 12 monthly averaged residuals at Midway and Tae-Ahn to the change in the March aggregated Asian source.

and the biomass burning sources are aggregated over Asia. By looking more closely at the “new” observation matrix \mathbf{H} , it is possible to get a better understanding of the impact of the Asian aggregated source on CO mixing ratios at the stations. Similarly, by looking more closely at the matrix $[\mathbf{H}^T \mathbf{R}^{-1} \mathbf{H} + \mathbf{P}_b^{-1}]^{-1} \mathbf{H}^T \mathbf{R}^{-1}$, it is possible to get a better understanding of the impact of the monthly mean residual observation vector $(\mathbf{y} - \mathbf{h}(\mathbf{x}^b))$ on the change in the Asian source, $(x^a - x^b)_{\text{March, Asia}}$.

[44] Figure 7 shows the modeled contribution of March Asian aggregated source to the monthly mean CO concentrations at Tae-ahn and at Midway (Pacific Ocean, 28N-177W). In the model, the biggest impact of this source on CO at the stations locations occurs at the Tae-ahn station, in the Korean peninsula, with a contribution to its mixing ratio in March of 53 ppbv. The largest contribution to CO mixing ratio at Midway (8.7 ppbv) occurs in April, the delay being due to the distance between the source region and the station location. The simulation using the a priori sources underestimates the CO mixing ratios, (compared to the observations), at Midway in March and April by 35 and 40 ppbv respectively and at Tae-ahn by 70 ppbv (Figure 6). As seen on Figure 7, the contributions of the aggregated source become almost negligible at both stations after June. The contributions are set to zero from September to February since we assume a 6 months impact timescale.

[45] Following the equation (1) from section 3.2 (see also Appendix C), the change in the Asian aggregated flux in March, $(x^a - x^b)_{\text{March, Asia}}$, is a weighted sum of the differences between the observed and modeled mixing ratios at each station (i.e., the residual vector $\mathbf{y} - \mathbf{h}(\mathbf{x}^b)$). More precisely, the difference between the a posteriori and the a priori Asian aggregated fluxes in March is the product of the corresponding row in the matrix $[\mathbf{H}^T \mathbf{R}^{-1} \mathbf{H} + \mathbf{P}_b^{-1}]^{-1} \mathbf{H}^T \mathbf{R}^{-1}$ (of dimension (N_x, N_y)) times the residual vector (of dimension N_y). Figure 7 shows the contribution of Tae-

ahn and Midway residual subvectors $(\mathbf{y} - \mathbf{h}(\mathbf{x}^b))_{\text{at Tae-ahn}}$ and $(\mathbf{y} - \mathbf{h}(\mathbf{x}^b))_{\text{at Midway}}$ (of dimension 12) to the change in the Asian aggregated source in March. Among all stations (not shown), the Midway residual subvector has the biggest impact. Its contribution to $(x^a - x^b)_{\text{March, Asia}}$ is +69 TgCO/yr, which corresponds to approximately 10% of the total increase of March Asian flux. Tae-ahn contribution is +5.3 TgCO/yr. As a consequence, at least 10 stations contribute to the peak and thus “constrain” the Asian source in March, making this inversion result more robust. As seen on Figure 7, the contributions of Tae-ahn and Midway residual subvectors can be negative, representing a decrease in the Asian emissions in March. The following lines give some further explanations. As seen on Figure 7, the model significantly under-estimates CO mixing ratios at Tae-ahn and Midway in spring. The February residual at Tae-ahn is 61.4 ppbv. In the inversion, this residual contributes to a 48.45 TgCO/yr increase in the February emissions over Asia (the total increase of the Asian emissions in February is 401.5 TgCO/yr). The direct effect of this increase is to reduce the CO mixing ratio residual (computed with the “new” sources) at Tae-ahn in February but also in March since CO lifetime is greater than one month at these latitudes in spring [Holloway et al., 2000]. As a result, the contribution of the February residual at Tae-ahn to $(x^a - x^b)_{\text{March, Asia}}$ is negative (−17.52 TgCO/yr) and cancels out part of the positive contribution of March residual at Tae-ahn (+39.85 TgCO/yr).

[46] For the two sets of a posteriori sources presented above, the major difference is in the Asian source. The a posteriori fluxes for the different processes in the Southern Hemisphere are not affected by the change in the Asian a priori uncertainty (not shown). In both cases the peak in the forest and savanna burning emissions over the Southern American and Southern African continents occurs one month earlier than in the prior. Moreover, even though the emissions due to agricultural waste burning and fuel-

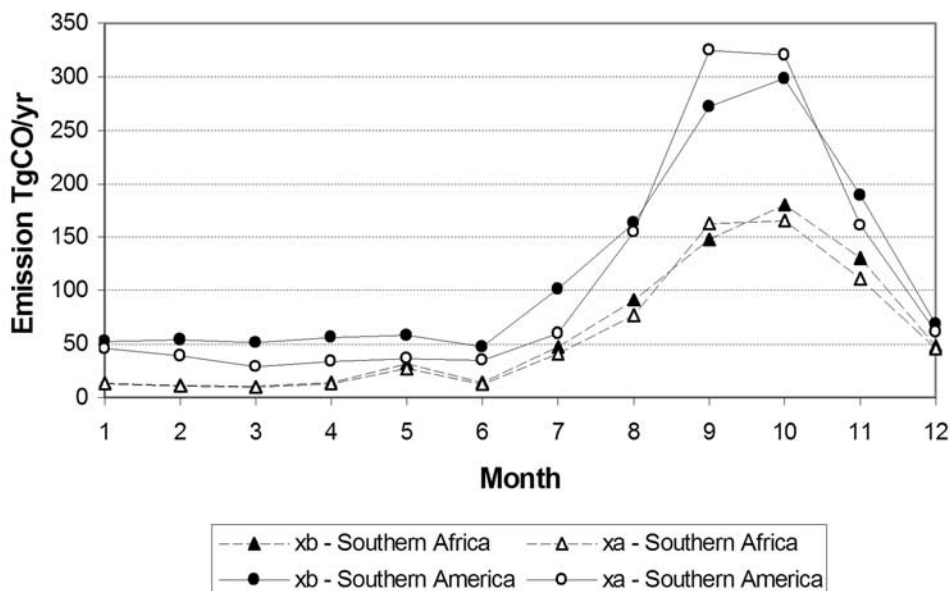


Figure 8. A priori (xb) and a posteriori (xa) monthly emissions due to forest and savanna burning over Southern Africa (triangles) and Southern America (circles).

wood were kept constant throughout the year over all regions in the a priori estimates, in the analysis these emissions clearly show a seasonal cycle and reach their peak during the respective winter-spring months of the considered Hemisphere.

[47] The timing of the maximum for the a posteriori CO emissions due to forest and savanna fires disagrees with *Hao and Liu* [1994] for the Southern American and Southern African continents. In this study, the a posteriori estimates for these sources already peak in September instead of October (see Figure 8). Similarly, *Bergamaschi et al.* [2000a, 2000b] shifted the seasonality of their global biomass burning a priori source (also based on *Hao and Liu* [1994]) by one month, based on the work of *Dwyer and Gregoire* [1998]. *Galanter et al.* [2000] recently proposed some corrections to the *Hao and Liu* [1994] inventory, dividing the various continents by ecosystem, with more detail than in the previous study and using remote sensing data to time the peak of emissions. They also found that the biomass burning emissions peak occurs earlier in Southern Africa. As an indication that the shifting of the emission peak improves the agreement between the observed and the modeled CO mixing ratios, Figure 9 displays the monthly mean observed CO mixing ratios at Ascension Island (8S - 14W) together with the modeled CO mixing ratios obtained with the a priori sources (\mathbf{x}^b) and the first inversion a posteriori sources (\mathbf{x}^a). With the a posteriori emissions set, \mathbf{x}^a , the model reproduces slightly better the observed seasonal cycle (timing and amplitude). As seen on Figure 9, CO due to chemical production in the model accounts for half to two-thirds of the total modeled CO mixing ratio at the station location. The seasonality though is mostly due to the contributions of CO direct sources. The a posteriori sources (\mathbf{x}^a) decrease the root mean square difference (RMSD) between the monthly mean observed and modeled CO mixing ratios at Ascension Island from 9.48 to 6.09 ppbv. To reduce even more the disagreement between the modeled and the observed CO at Ascension Island, the

biomass burning emissions over Southern America should be increased in August and September. The inversion does not calculate such an increase, due to the fact that this change would not further decrease the global RMSD. Indeed, the increase of biomass burning emissions in the Southern hemisphere leads to higher RMSD at the stations located in Antarctica: South Pole, Palmer station, Syowa.

[48] *Holloway et al.* [2000] studied the model response to the OH field and explained that away from major source regions, CO is more sensitive to OH (and to transport than to emissions). Using the measurements at the ALE-GAGE stations (see description given by *Prinn et al.* [2000]) between 1978 and 1994, *Prinn et al.* [1995] derived new estimates for the trichloroethane, CH_3CCl_3 , (total) lifetime and the methane lifetime due to the reaction with OH. These estimates for the total atmosphere are 4.8 ± 0.3 years and 8.9 ± 0.6 years respectively. The authors also show that OH concentrations have not substantially changed from 1978 to 1994. Using the same data set as *Prinn et al.* but a different method, *Krol et al.* [1998] obtained quite different results for the period 1978 to 1993. Their estimate for OH concentration trend was $0.46 \pm 0.6\%/yr$. They also computed the global lifetime of trichloroethane in the troposphere to have changed from 4.7 ± 0.1 yr in 1978 to 4.5 ± 0.1 yr in 1993 and the methane lifetime due to the reaction with OH to have changed from $9.2^{+1.7}_{-0.8}$ yr in 1978 to $8.6^{+1.6}_{-0.8}$ yr in 1993. The global photochemical lifetime of methane in the troposphere deduced from a full chemistry and transport model simulation using the a posteriori CO surface sources is 8.74 years, to be compared with 8.42 years in the simulation with the a priori CO surface sources. The global lifetime of CH_3CCl_3 in the troposphere, is 4.41 years to be compared with 4.27 years in the simulation with the a priori CO surface sources. The comparison of these different lifetimes values shows that the IMAGES model running with the a posteriori CO surface sources agrees better with the *Prinn et al.* and *Krol et al.* estimates, even though these two studies obtained different conclusions

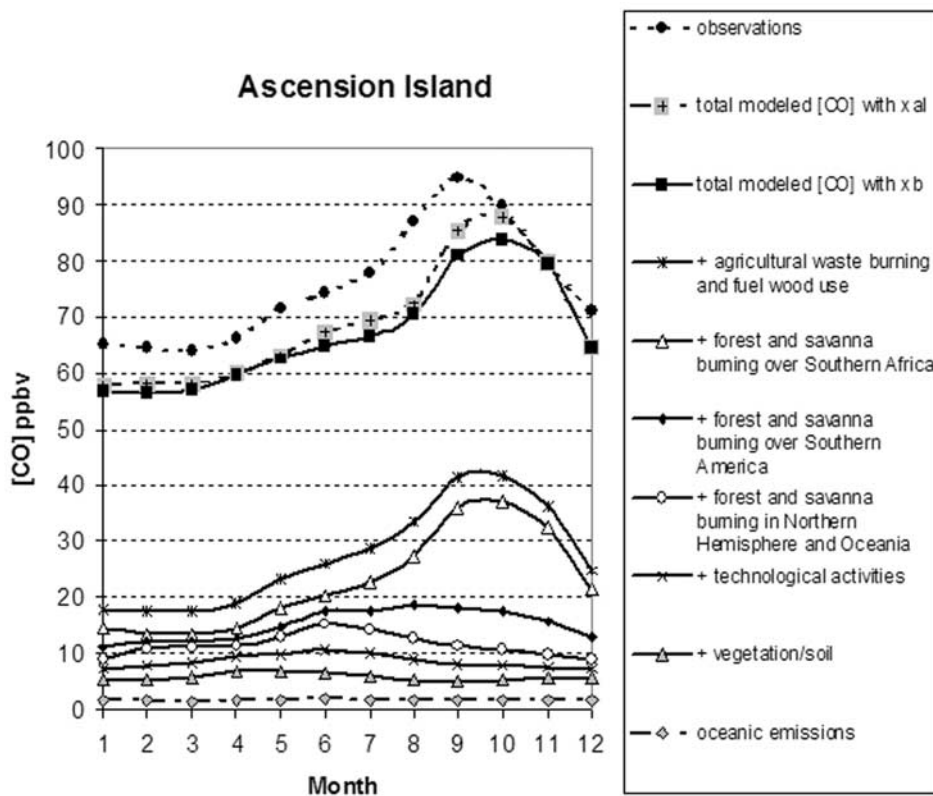


Figure 9. Observed and modeled monthly averaged CO mixing ratio, at Ascension Island (7.92S, 14.42W). The 33 tagged contributions to the simulated mixing ratio are added up with first the oceanic emissions, then the emissions due to vegetation/soils, the emissions due to technological activities, the emissions due to forest and/or savanna fires, and, finally, the emissions due to fuelwood use and agricultural waste burning. The simulated [CO] chemically produced is added to [CO] due to surface emissions to get the total modeled [CO] with the a priori sources \mathbf{x}^b . The total [CO] obtained with the a posteriori sources \mathbf{x}^a and the monthly averaged CMDL observations are also shown.

using the same data set (see, for a detailed discussion, *Prinn and Huang* [2001] and *Krol et al.* [2001]). This is not sufficient either to validate the OH fields computed by IMAGES or to support the a posteriori CO surface sources since the global lifetime of CH_3CCl_3 mostly contains information about OH in the tropics,.

[49] One way to validate the inversion results is to calculate the root mean square difference between the monthly mean observed and modeled CO mixing ratios at all stations. The RMSD obtained using the a priori set of sources is 30.47 ppbv. When using the linear version of the model and the first inversion results, the new (“linear”) RMSD computed is 17.56 ppbv (the modeled CO is here expressed as $\mathbf{h}(\mathbf{x}^b) + \mathbf{H}(\mathbf{x}^a - \mathbf{x}^b)$). In order to estimate the importance of the chemical feedback (impact of CO on OH and hence on its chemical lifetime), the full model was run in a 2-year-long simulation with the a posteriori sources obtained in the first inversion, thus long enough to allow the OH field to adjust to the new set of emissions. The new RMSD (the modeled CO is now expressed as $\mathbf{h}(\mathbf{x}^a)$) is 17.73 ppbv. It is very close to the “linear” RMSD of 17.56, showing that the nonlinearity of the problem is reasonably weak.

[50] A second iteration of the inversion has been performed to check the impact of the new sources on OH, and its feedback on CO distribution. This inversion uses the a posteriori fluxes from the first analysis, \mathbf{x}_1^a , as the new a

priori sources. A simulation with the full chemistry model and the new CO direct sources has been performed to compute the new OH fields. These fields were read by the tracer version of the model to compute the new observation matrix \mathbf{H}_1 . The expression to calculate the new a posteriori sources, \mathbf{x}_2^a , is taken from *Tarantola and Valette* [1982b] generalization to the nonlinear case of the inverse problem solution:

$$\mathbf{x}_2^a = \mathbf{x}_1^a + [\mathbf{H}_1^T \mathbf{R}^{-1} \mathbf{H}_1 + \mathbf{P}_b^{-1}]^{-1} \{ \mathbf{H}_1^T \mathbf{R}^{-1} (\mathbf{y} - \mathbf{h}(\mathbf{x}_1^a)) - \mathbf{P}_b^{-1} (\mathbf{x}_1^a - \mathbf{x}^b) \} \quad (3)$$

\mathbf{H}_1 is the new observation matrix calculated by linearizing the model around the first analysis solution, \mathbf{x}_1^a , so that the system to be solved can be written: $\mathbf{y} = \mathbf{h}(\mathbf{x}_1^a) + \mathbf{H}(\mathbf{x} - \mathbf{x}_1^a) + \epsilon$.

[51] The results of the second iteration are shown in Table 2, last columns. The total for each process differs from the first inversion results (Table 2) by less than 6%. As expected, the estimates of regional fluxes responsible of high CO mixing ratios at stations in their downwind flow can be substantially affected by the nonlinearity of the CO-OH chemistry.

4.2. Sensitivity Studies

[52] The inversion of surface sources aims not only at optimizing fluxes by minimizing the deviation of the model

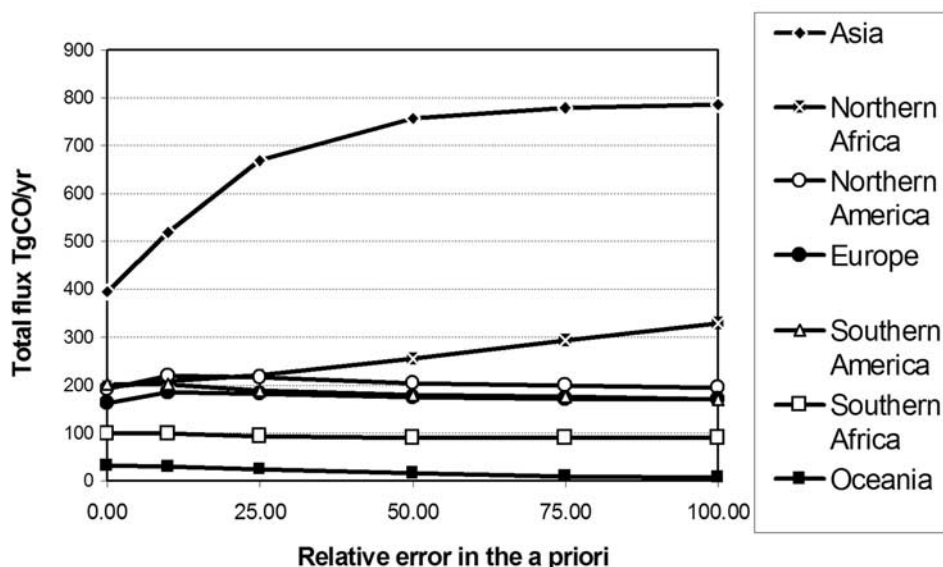


Figure 10. Impact of the relative errors in the a priori fluxes on the analyzed fluxes over the 7 continental regions considered.

from the observations, but it also aims at reducing the uncertainty on the fluxes values. As the number of parameters to optimize increases, the error in the a posteriori estimates does not decrease as much. Clearly, increasing the number of the unknowns, while keeping the same set of observations, reduces the constraint on each unknown [Enting *et al.*, 1995; Enting, 1993]. As a result, to substantially reduce the uncertainty on the analysis, it is necessary to adjust the number of parameters to be optimized.

[53] In this section, the inversion is performed on monthly total surface fluxes. The emissions due to the 4 continental processes tagged in the previous sections are now aggregated into one single flux over each continent. Over each region, the uncertainty attached to the total flux is arbitrarily set to 50% of its a priori value. The annual results for this new “control inversion” are presented in Table 3 (columns 4 and 5). They agree quite well with the regional sum of annual a posteriori fluxes from the first inversion analysis shown in Table 2 (except for Oceania), which shows the consistency of the inverse method for regions which are well constrained by the network. The Asian and Northern African fluxes are bigger in the control inversion by 7% and 14% respectively. The flux over Oceania is down to 15.3 TgCO/yr in the control inversion, to be compared with 27.7 TgCO/yr in the first inversion. The other fluxes differ by less than 3%. The new (“linear”) RMSD value is 17.56 ppbv, which is exactly equal to the global linear RMSD computed when using the emissions from the first analysis (section 4.4).

[54] A major source of uncertainties for the inversion of sources is the transport model [Bousquet *et al.*, 1999a, 1999b]. The results of the inversion depend on the model spatial resolution (horizontal and vertical), on the convection scheme, on the winds used for the forcing, on the subgrid-scale mixing representation (diffusion, convection). As the transport in IMAGES is based on a monthly averaged climatological parameterization, it is not used to study a specific year of data or the interannual variability of observations. The spatial resolution of the model is also

rather coarse. The model consequently does not capture either local and short events or fine vertical gradients. We consider that our model results are less affected by local pollution than can occur at observations location. The influence of the transport model on the results has not been quantified in this study.

[55] Besides the transport model, there are other sources of errors for the inversion results. The a priori information used in the inversion scheme has a great influence on the a posteriori sources and their uncertainties. To test the influence of the values given to the a priori 396 CO emission fluxes, random 0% up to 20% relative perturbation are added to the values used as a priori sources in the previous inversions. Ten inversions have been performed with perturbed a priori fluxes, keeping everything else as in the “first” inversion (presented in section 4.4). For the 10 inversions, the a posteriori global annual fluxes obtained deviate from the unperturbed inversion results by less than 4%. The difference in the annual regional a posteriori surface fluxes is less than 10% in all regions except for Northern America (<13%) and Northern Africa (<20%). This shows that while the inversion results depend on the fluxes a priori values, the a posteriori fluxes for most regions stay quite close to the first inversion results. The information contained in the observations provides a good constraint for these fluxes, especially for the global and annual CO surface source.

[56] In the next experiment, everything is set up as in the previous inversion scheme, except that the a priori fluxes relative errors now vary and are successively set to 10, 25, 50, 75, 100% of the fluxes a priori values. Figure 10 shows the impact of the a priori relative error on the annual a posteriori total fluxes for the 7 continental regions. The values at 0% relative error correspond to the values of the a priori fluxes. The behavior of the curves suggests a range of uncertainty for the fluxes. Total fluxes over Northern Africa and Oceania are the most influenced when a priori errors are larger than 25%. The other fluxes tend to reach a stable value when relative errors are above 50%. The relative

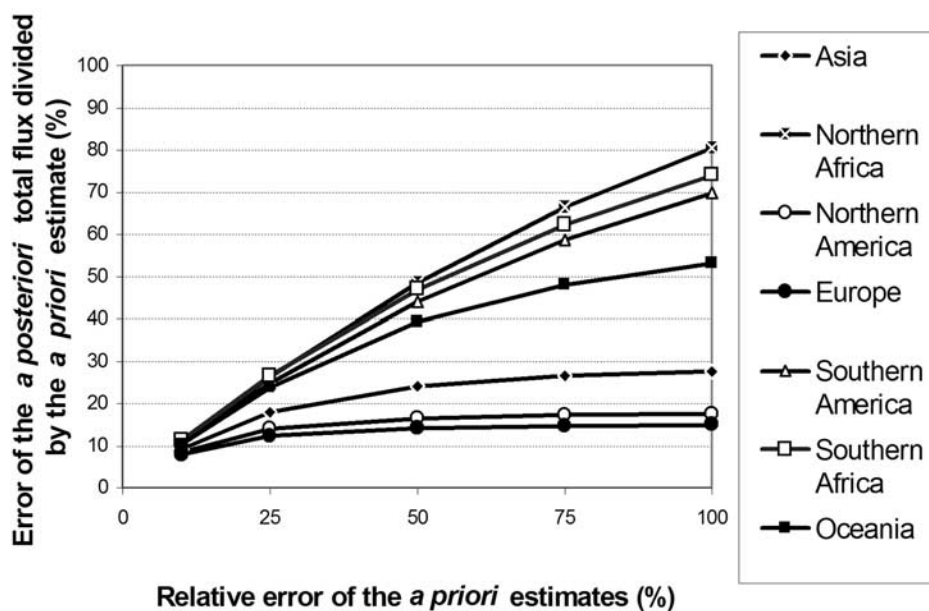


Figure 11. Impact of the relative errors in the a priori fluxes on the analyzed fluxes uncertainties for the 7 continental regions considered.

errors attached to the a posteriori total fluxes are given in Figure 11. For all fluxes, a posteriori absolute errors are equal to or smaller than the a priori absolute error values. The regions for which the uncertainty on the total flux decreases the most (Europe, Northern America and Asia) are best constrained by the CMDL network. This is in large part due to the fact that 17 stations out of 39 are located between 30°N and 60°N . With 100% uncertainty on the a priori surface fluxes, the relative uncertainty on the a posteriori (for each region: a posteriori error divided by the a posteriori estimate) is as low as 14.4% for Europe, 13.9% for Asia and 17.3% for Northern America, whereas it is as high as 230% for the flux over Oceania.

[57] The high relative uncertainty in the flux over Oceania is due to a bias in the inversion method. On one hand, the variability of the observations at Cape Grim (Tasmania) is underestimated since the measurements are filtered to only sample marine air. On the other hand, the averaged modeled concentrations at Cape Grim are over-estimated since no filtering is applied on the modeled outputs. This bias will be reduced when observed winds are used in the transport model and the same filtering is applied to the observed and to the modeled sampled mixing ratios.

[58] In the next inversion, the 396 monthly surface fluxes as well as the annual and global production of CO due to methane oxidation, $P_{\text{CH}_4}(\text{CO})$, and the annual and global production of CO due to the non methane hydrocarbons oxidation (isoprene, terpenes, ...), $P_{\text{NMHC}}(\text{CO})$, are optimized. The a priori relative errors on the two production terms are set to 50%. All the other statistics are taken as in the first inversion performed in section 4.1. The two productions a posteriori values are 1121 TgCO/yr and 161 TgCO/yr respectively, which is unrealistic. When the a priori relative error on $P_{\text{CH}_4}(\text{CO})$ is set to 1%, the two production terms a posteriori values are 740 TgCO/yr and 660 TgCO/yr respectively. The inversion scheme used here does not seem

to be able to differentiate between the two production terms. The cosine of the angle between the two column-vectors corresponding to the $P_{\text{CH}_4}(\text{CO})$ and $P_{\text{NMHC}}(\text{CO})$ contributions at the stations in the observation \mathbf{H} matrix is 0.9755. This value very close to 1 confirms the fact that the normalized impacts of the two production terms are almost identical in the model and consequently only the total chemical production of CO, $P(\text{CO})$, can be optimized. Using almost the same scheme as before but now with the total and annual chemical production of CO, $P(\text{CO})$ a posteriori value is 1461 TgCO/yr and the attached uncertainty has not decreased. The a posteriori global surface emission value, resulting from the same inversion, is 1590 TgCO/yr. For the next inversion, the control scheme, from section 4.2, is used to optimize the monthly total surface fluxes for the 12 regions considered before, as well as the global and annual chemical production of CO. The a posteriori value for CO production is 1536 ± 41 TgCO/yr and the a posteriori global and total CO surface flux is 1528 TgCO/yr. The results per region are given in the last two columns of Table 3. The total source of CO is quite similar for the two inversions presented in this table (3045 and 3064 TgCO/yr). The increase in the chemical production of CO obtained in the last inversion is compensated by a decrease in the fluxes over all continental regions, except over Europe.

[59] As a consequence, to better separate the surface emissions and the chemical production of CO in the inversion, more data (total CO and isotopic ratios, measurements closer to the emissions location) are needed as well as improved inventories of CO precursors emissions. In the present study, the a posteriori direct global emissions of CO ranged from 1528 to 1694 TgCO/yr and the chemical production of CO changed from 1373 when fixed to 1461–1536 TgCO/yr when optimized. These values are in the high end of the Kanakidou *et al.* [1999] range as well

Table 3. Regional Total Fluxes and Their Uncertainties^a

Region	A Priori		Without Optimizing P(CO)		Optimizing P(CO) As Well	
	Annual Emission Flux	A Priori Uncertainty	A Posteriori Annual Emission Flux	A Posteriori Uncertainty	A Posteriori Annual Emission Flux	A Posteriori Uncertainty
Europe	162.6	81.3	174.9	23.1	173.2	23.2
Asia	395.2	197.6	756.3	95.7	719.5	96.2
Northern Africa	197.4	98.7	255.4	96.0	226.3	96.4
Southern Africa	98.4	49.2	90.2	46.2	75.47	46.4
Oceania	31	15.5	15.3	12.2	12.11	12.3
Northern America	192.7	96.3	204.7	31.9	190.2	32.2
Southern America	202.2	101	180.1	89.1	114.7	90.9
Oceans	16.4	4.0	16.7	4.0	16.2	2.9
Global surface emissions	1296		1694		1528	
Global chemical production	1373	686.5	Not optimized (1373)		1536	41
Total source	2669		3067			3064

^aRegional total fluxes and their uncertainties are given in TgCO/yr. Shown here are (1) a priori values (columns 2 and 3), (2) a posteriori values for the inversion of regional and monthly surface total fluxes (columns 4 and 5) and (3) a posteriori values for the concomitant inversion of regional and monthly surface total fluxes and the global annual chemical production of CO.

as the *Bergamaschi et al.* [2000a] range. Most of the increase in CO surface source occurred over Asia. Such an increase has not been reported before, except for a 15.7% increase of CO emissions in China between 1990 and 1995 (99 to 115 TgCO/yr; *Streets and Waldhoff* [2000]). Such accurate estimates of CO emissions in the other countries of our Asian region are not available at present. Future studies and inventories should help validate inversion results.

4.3. Comparison With Other Studies

[60] Our method is first compared with *Bergamaschi et al.* [2000a, 2000b] time-independent approach. The seasonality of all sources is fixed and the inversion scheme is modified to only optimize the annual and global surface sources for 5 processes. *Bergamaschi et al.* used data from 31 CMDL stations for the year 1994. Here, we use the same observations as considered before at the 39 CMDL stations. *Bergamaschi et al.* used different a priori sources and categories: they aggregated the CO biogenic direct emissions with the biogenic indirect source, adding another 100 TgCO/yr to this last source a priori value. Their total annual surface a priori source was 1470 TgCO/yr (+100) compared with 1296 TgCO/yr in this study. In the time-independent inversion scheme, relative errors of 50% are put on all global sources except for the technological one, the uncertainty of which is put at 10%. The total a posteriori surface source obtained by *Bergamaschi et al.* ranged from 1347 TgCO/yr to 1560 TgCO/yr, depending on the OH field, the wind field, the number of stations they used. The results of our time-independent inversion (to be compared with the last row of Table 2) are as follow: emissions due to technological activities increase from 294 to 309 TgCO/yr, emissions due to forest and savanna burning increase from 436 to 606 TgCO/yr, emissions due to agricultural waste burning and fuelwood use increase from 384 to 561 TgCO/yr, soil-vegetation and oceanic emissions slightly increase from 165 to 167 TgCO/yr and from 16.5 to 20 TgCO/yr respectively. Consequently, the a posteriori total surface flux of 1663 TgCO/yr obtained here compares well with the highest *Bergamaschi et al.* estimate (1560+ 100 TgCO/yr). With the new annual and global values for the

fluxes, the RMS of the observed minus modeled CO mixing ratios at the stations is 21 ppbv, which is 2/3 of the RMSD obtained with the a priori emissions. Hence, even if we do not correct either for the seasonality or for the spatial distribution of the emissions, changes in the global and annual fluxes already significantly decrease the distance between the observed and the modeled CO mixing ratios at the stations.

[61] Table 4 shows the global and annual budget of CO as reported in published forward or inverse studies. For the inverse studies (*Bergamaschi et al.* [2000a] and this study), the a priori sources and the range of the a posteriori sources are given. The forward studies include the GIM/IGAC intercomparison performed in 1997 [*Kanakidou et al.*, 1999] and the study of CO global distribution by *Holloway et al.* [2000]. The GIM/IGAC intercomparison evaluated the performance of eleven 3-D chemistry and transport models in reproducing the tropospheric ozone chemistry. *Kanakidou et al.* [1999] reported the results for the distributions of CO, which is the best documented precursor of ozone. Part of the differences in the modeled CO distributions was due to the fact that the models used different emissions for CO and its precursors. For the 11 models, the direct global emissions of CO ranged from 1040 to 2362 TgCO/yr and the chemical production of CO ranged from 840 to 1459 TgCO/yr, this upper limit corresponding to the IMAGES model (1997 version). For comparison, in the full IMAGES (2001) model run with the a priori emissions, the total chemical production of CO is 1373 TgCO/yr, of which 735 TgCO/yr are due to methane oxidation. In the *Holloway et al.* [2000] study, the sum of all CO sources used in the GFDL model was 2491 TgCO/yr. They used fixed monthly OH fields derived from *Spivakovsky et al.* [1990], which they increased by 15% to agree with *Prinn et al.*'s [1995] 4.8 years estimate of trichloroethane lifetime. The authors point out that the fossil fuel sources (300 TgCO/yr) could be too low as their model significantly under-estimates the spring peak in CO mixing ratios at higher northern latitudes. This feature also appeared in the CO distribution obtained with IMAGES using the a priori emissions. Indeed the transport in the Arctic region is not always well reproduced by models, especially during the

Table 4. Comparison of CO Budgets From Four Different Studies

TgCO/yr	This Work		<i>Bergamaschi et al.</i> [2000a] ^a		<i>Holloway et al.</i> [2000] ^b	<i>Kanakidou et al.</i> [1999]
	A Priori	A Posteriori	A Priori	A Posteriori		
Direct source	1296	1528–1694	1470	1347–1565	1048	1040–2362
Indirect source						
CH ₄	735		830		760	
NMHC	638		560		683	
Total	1373	1461–1536	1390	1391–1653	1443	840–1459
Total source	2669	2960–3067	2860	2867–3009	2491	1218–2742

^a*Bergamaschi et al.* [2000a] aggregated the CO direct biogenic emission with the biogenic NMHC source, adding 100 TgCO/yr to the indirect source of CO (and thus reducing the direct source).

^bThree sources included in this study were not taken into account in the *Holloway et al.* [2000] CO budget. These sources are as follows: CO due to the oxidation of anthropogenic NMHC, CO emitted by the vegetation and soil and CO emitted by the ocean. Given estimates by *Kanakidou and Crutzen* [1999] and *Granier et al.* [2000a], these sources would add up to 280 TgCO/yr.

winter-spring season. Errors in the transport model probably explain part of the mismatch between the modeled and the observed CO distributions over the Arctic region in spring. It is nevertheless difficult to estimate how much of the disagreement is due to errors in the transport model and how much is due to errors in the emissions. In this study, the disagreement is for a great part corrected when using the a posteriori fluxes from section 4.1 (Figure 6). The RMSD at Alert, Barrow, Cold Bay, Heimaey, Mould Bay and Shemya Island are divided by a factor ranging from 2.5 to 6. The a posteriori fluxes lead to a very small number of increase in the disagreement at the Northern latitudes: Baltic, Mace Head and Key Biscayne are the three stations where the RMS of the modeled minus the observed CO mixing ratios increases with the a posteriori fluxes. The improvement at most surface and remotely located stations may be misleading. Higher emissions in one region may be compensating errors in the transport model and errors in other sources. The use of models running with observed winds together with measurements (surface and vertical profiles) taken downwind of and close to the emissions location could prevent errors in the transport model and in the OH field from having a strong influence on the inversion results.

[62] *Granier et al.* [2000a] and *Holloway et al.* [2000] showed that the contribution of methane oxidation to CO surface mixing ratio does not significantly vary with the season and the latitude. Most of the uncertainty lays in the CO yield of methane oxidation. *Holloway et al.* [2000] model over-estimated CO over Antarctica, more especially during the peak of biomass burning and biogenic emissions. The authors first suggested that this could be (partly) due to the CO yield assumed for the methane oxidation. They also proposed that the biomass burning and biogenic emissions in the South hemisphere could be too high in their model. When *Bergamaschi et al.* [2000b] incorporated ¹²C/¹³C ratios in their inverse scheme, their results indicated that CO yield from methane oxidation is likely to be significantly lower than 1. In the *Holloway et al.* [2000] study, the yield was 1, and in the *Kanakidou and Crutzen* [1999] study, it was 0.9. The carbon yield for CO due to the oxidation of methane is 0.82 in our study. *Holloway et al.* [2000] reduced the carbon yield in their study from 1 down to 0.82. This changed the source of CO due to the oxidation of methane from 760 TgCO/yr down to 623 TgCO/y. The direct effect was to decrease CO modeled mixing ratios in

Antarctica and Tasmania by 4 ppbv, which lead to a generally better agreement and also to a slight under-estimate of CO in the first months of the year. With the a priori sources, the IMAGES model reproduces quite well the CO mixing ratios at the most Southern stations (see Figure 6). With the first a posteriori emissions set described in section 4.1, the IMAGES model still reproduces quite well the CO mixing ratios over Antarctica but only during half of the year. The increased emissions during the biomass burning peak season of the Southern Hemisphere results in a slight over-estimation of CO over Antarctica from August to February. These results tend to show that the Southern hemisphere biomass burning emissions in the *Holloway et al.* [2000] model could be responsible for the misfit between the observations and the modeled CO. It clearly appears here that the inverse modeling approach can complement forward studies. Indeed the inversion deduces, from data and the forward model, the fluxes to be changed to improve the agreement between the model and the observations.

[63] *Novelli et al.* [1994] estimated that 23% (44%) of total atmospheric CO in the Northern (Southern) Hemisphere is provided by methane oxidation. In another study using the IMAGES model [*Granier et al.*, 2000a], the oxidation of methane contributed to 28% of the total content of CO. This is close to *Novelli et al.* [1994] values, considering that, in the IMAGES model, almost 60% of CO atmospheric burden (310 Tg) is in the Northern Hemisphere. Methane oxidation clearly fixes a “background” level for CO at all stations. In section 4.2, we showed that our method does not allow us to decrease the uncertainty on the contribution to CO of methane oxidation alone. In IMAGES, this contribution is 735 TgCO/yr (when using the a priori CO emissions). The methane oxidation contributions given by *Holloway et al.* [2000], *Bergamaschi et al.* [2000b] and *Kanakidou and Crutzen* [1999] are in the same range.

5. Conclusion

[64] In this study, we presented how the concept of states of information has been used in a 3-D synthesis time-dependent inversion technique to optimize CO surface emissions. Outputs from the climatological model IMAGES have been compared with monthly averaged measurements of CO mixing ratios over the period 1990–1996 at 39

stations from the CMDL network. The discrepancies between the observed and the modeled CO mixing ratios at the stations location were minimized by optimizing the monthly surface CO fluxes over 5 oceanic regions and over 7 continental regions for 4 different processes (technological activities, forest and savanna burning, fuelwood use and agricultural waste burning, vegetation/soils).

[65] The surface CO emission fluxes have been optimized over each continent for 4 different processes and on a monthly basis. The spatial distribution inside each region and for each process was fixed. The time-dependent inversion technique proves to be a powerful tool to study the intensity and the seasonality of each emission process, supposing a sufficient number of observations are available. As tested by *Peylin et al.* [1999] for CO₂, the inversion scheme is able to retrieve the origins of a tracer observed at a network of stations.

[66] The 1990 a priori estimate of the CO total flux over Asia is significantly lower than the optimized flux obtained using the observations. The inversion results also showed a different timing for the biomass burning emission peak over Southern Africa and Southern America. By shifting the maximum one month earlier (September instead of October), the modeled CO mixing ratio at Ascension agrees better with the observations, which peak in September. The synthesis inversion technique cannot change the location of the sources inside the regions. It only optimizes the magnitude of each emission process over each large region. Further studies will use different emission inventories to test the impact of the sources location. To optimize the location of the emissions and supposing enough observations are available, adjoint models should be used since they can be designed to optimize the fluxes on the forward model grid scale [*Kaminski et al.*, 1999a, 1999b; *Houweling et al.*, 1999].

[67] Although it is clear that a posteriori results depend on the winds fields and on the convection parameterization in the model, in the present study, the errors associated with the transport model are not considered. As noted before, measurements from CMDL coastal sites (MHD, CGO, KEY) are filtered to sample only oceanic air. In a study presenting key issues for the improvement of methane sources inversion, *Houweling et al.* [2000] showed how critical it is to use observed winds in the CTM and to apply the wind sector filtering to the model data. In further studies, these two requirements should be fulfilled.

[68] The emissions of CO precursors have been specified, except in the last experiment. In the last two inversions, the annual and global production of CO due to methane and NMHC oxidation was optimized together with the surface fluxes of CO. In the model, the oxidations of CH₄ and NMHC have quite similar impacts at the stations, making it difficult to optimize both of them separately with CO data only. *Bergamaschi et al.* [2000b] showed that the introduction of ¹³C/¹²C and C¹⁸O/C¹⁶O isotopic data in the inversion scheme helps better constrain CO surface emissions and the CO global yields from the oxidation of various hydrocarbons. As more measurements of isotopic signatures of emissions and of isotopic fractionation by reactions become available, the comparison between data and the distribution of stable isotopes computed by models should further constrain the global budget of CO.

[69] Many factors in the models affect the distribution of CO, the emissions used as boundary conditions being one of them. For further intercomparison studies, all models should use the same set of emissions and include a comparison of their OH distributions. Errors in one type of emission can indeed be compensated by errors in other sources, in the transport or in the OH field. The total source of CO in IMAGES is in the high end of the range reported by *Kanakidou et al.* [1999]. The CO total source reported by *Holloway et al.* [2000] is quite close to our total a priori source: 2500 TgCO/yr and 2669 TgCO/yr respectively. The carbon yield for CO due to the oxidation of methane is different in both studies: ranging from 0.82 to 1. However, the source of CO due to the oxidation of methane is close to 750 TgCO/yr in both models. More studies on CO secondary sources should help improve the model chemistry schemes and thus the inversion results.

[70] The inverse modeling technique described here provides a good diagnostic tool to assess CO surface emissions at the continental scale. If sufficient observations become available and with appropriate additions/improvements in the models, the inverse modeling experiments can also be designed to help characterizing the emission processes. As explained in section 4.1, the inversion of 33 CO surface fluxes using 39 CMDL stations is a poorly constrained problem for several emissions. The few continental stations sampling downwind of land sources are located in Europe (Baltic Sea, Poland; Gozo, Malta; and Hegyhatsal, Hungary), in the USA (Park Falls, Wisconsin; Niwot Ridge, Colorado; and Wendover, Utah), and Asia (Ulaan Uul, Mongolia, and Qinghai Province, China). Given its 2 months average lifetime, CO is a good tracer for synoptic events. Despite the presence of 4 stations in the Southern Hemisphere tropics, emissions due to biomass burning in Africa and Southern America are poorly sampled. Consequently, the corresponding a posteriori fluxes are mostly constrained by the a priori values and the uncertainties in the fluxes do not significantly decrease (Table 3, see columns 2 and 3). The extension of the regular measurement operations to sites downwind of major source regions, as well as the improvements of emissions inventories using bottom-up and top-down approaches, are two important initiatives to be encouraged. Inverse modeling studies using higher resolution models and observed winds could be used to indicate where new observation sites should be located to help better constrain emissions.

[71] The advantage of the top-down approach is that fluxes can be estimated over large areas. The disadvantage is that it does not bring any direct information about the mechanisms driving the sources. To better describe each process source, smaller regions with homogeneous land cover, industrial development and activities, population densities, climatology should be used for the inversion. Nevertheless, the number of surface fluxes that may be optimized is greatly limited by the number and the quality of the available observations.

[72] Further studies will employ assimilated meteorology and higher resolution CTM to optimize CO sources (seasonality as well as spatial distribution) using the limited but high quality measurements at surface stations as well as the

newly available satellite observations (IMG, Clerbaux *et al.* [2001]; MOPITT, Drummond [1992]).

Appendix A: Characterization of the Properties of the Linear System $\mathbf{y} = \mathbf{h}(\mathbf{x}^b) + \mathbf{H}(\mathbf{x} - \mathbf{x}^b) + \boldsymbol{\varepsilon}$

[73] As first explained in section 3.2, the system $\mathbf{y} = \mathbf{h}(\mathbf{x}^b) + \mathbf{H}(\mathbf{x} - \mathbf{x}^b) + \boldsymbol{\varepsilon} = \mathbf{H}\mathbf{x} + \mathbf{y}_{\text{chem}} + \boldsymbol{\varepsilon}$ (with $\mathbf{y}_{\text{chem}} = \mathbf{h}(\mathbf{x}^b) - \mathbf{H}\mathbf{x}^b$) is over-determined, since there are more observations than unknowns ($N_y > N_x$). Out of the 33 fluxes to be optimized monthly, 15 are in the Southern Hemisphere and out of 39 CMDL stations, 9 only are in the Southern Hemisphere. Given the lifetime of CO and the interhemispheric transfer time, measurements at most stations in the Northern Hemisphere do not carry much information on sources in the Southern latitudes. As a consequence, the problem is ill conditioned in the Southern Hemisphere and some continental sources are not sampled well by the network. A common technique to solve an ill-conditioned least square problem (with no prior) is to use the singular value decomposition (SVD) [Lanczos, 1961]. This decomposition is a handy tool to characterize the linear system properties. Using the SVD function, the \mathbf{H} matrix may be written as the product of 3 matrices $\mathbf{H} = \mathbf{U}\boldsymbol{\Lambda}\mathbf{V}^T$ where the columns vectors \mathbf{u}_j of $\mathbf{U}(N_y, N_y)$ form an orthonormal basis in the observations space, so that

$$\mathbf{y} = \sum_{j=1}^{N_y} \beta_j \mathbf{u}_j, \quad \mathbf{y}_{\text{chem}} = \sum_{j=1}^{N_y} \gamma_j \mathbf{u}_j$$

(the γ_j are fixed) and

$$\boldsymbol{\varepsilon} = \sum_{j=1}^{N_y} \delta_j \mathbf{u}_j$$

the columns vectors \mathbf{v}_i of $\mathbf{V}(N_x, N_x)$ form an orthonormal basis in the surface emissions space so that

$$\mathbf{x} = \sum_{i=1}^{N_x} \alpha_i \mathbf{v}_i;$$

and $\boldsymbol{\Lambda}$ is a rectangular matrix (N_y, N_x) so that

$$\boldsymbol{\Lambda} = \begin{bmatrix} \mu_1 & 0 & \cdots & 0 \\ 0 & \mu_2 & \ddots & \vdots \\ \vdots & \ddots & \ddots & 0 \\ 0 & \cdots & 0 & \mu_{N_x} \\ \hline & & & \mathbf{0} \\ & & & \vdots \\ & & & \mathbf{0} \end{bmatrix}$$

where $(\mu_i)_{i=1, N_x}$ is the singular value spectrum of \mathbf{H} . This decomposition is unique, except for trivial changes like permutations. The \mathbf{v}_i verify $\mathbf{H}\mathbf{v}_i = \mu_i \mathbf{u}_i$.

[74] Suppose $M \leq N_x$ is the number of singular values μ_i not equal to zero. By substituting \mathbf{x} , \mathbf{y} , \mathbf{y}_{chem} and $\boldsymbol{\varepsilon}$ in the system's equation [Wunsch, 1996; Haine, 2001], we obtain a new system where the unknowns are the $(\alpha_i)_{i=1, N_x}$ and the $(\delta_j)_{j=1, N_y}$:

$$\begin{aligned} \sum_{i=1}^{N_x} \alpha_i \mathbf{H}\mathbf{v}_i + \sum_{j=1}^{N_y} \gamma_j \mathbf{u}_j + \sum_{j=1}^{N_y} \delta_j \mathbf{u}_j &= \sum_{j=1}^{N_y} \beta_j \mathbf{u}_j \\ \Leftrightarrow \sum_{i=1}^M \alpha_i \mu_i \mathbf{u}_i + \sum_{j=1}^{N_y} \gamma_j \mathbf{u}_j + \sum_{j=1}^{N_y} \delta_j \mathbf{u}_j &= \sum_{j=1}^{N_y} \beta_j \mathbf{u}_j \end{aligned}$$

so that

$$\alpha_i \mu_i + \gamma_i + \delta_i = \beta_i \quad \text{for } i = 1, M \quad (\text{A1})$$

and

$$\begin{aligned} 0 + \gamma_i + \delta_i &= \beta_i \quad \text{for } i = M + 1, N_y \\ \Leftrightarrow \delta_i &= \beta_i - \gamma_i \quad \text{for } i = M + 1, N_y \end{aligned} \quad (\text{A2})$$

[75] If M is less than N_x , the coefficients $(\alpha_i)_{i=M+1, N_x}$ can be chosen arbitrarily, making the number of solutions infinite. For $i = M + 1, N_y$, the coefficients δ_i are determined from equations (A2). This leaves the first part of the system (A1) to be solved, with M equations and $2M$ unknowns the $(\alpha_i)_{i=1, M}$ and the $(\delta_i)_{i=1, M}$. Another piece of information is needed to solve the system: in the least squares approach, the deviation between the observations and the modeled data is minimized, which is equivalent to the minimization of $\boldsymbol{\varepsilon}$ norm, $(\boldsymbol{\varepsilon}^T \boldsymbol{\varepsilon})^{1/2}$. Since

$$\boldsymbol{\varepsilon} \boldsymbol{\varepsilon}^T = \sum_{j=1}^{N_y} \delta_j^2 = \sum_{j=1}^M \delta_j^2 + \sum_{j=M+1}^{N_y} (\beta_j - \gamma_j)^2,$$

the only way to minimize the sum is to take $\delta_i = 0$ for $i=1, M$. Using the SVD decomposition to solve the least squares problem gives the M first coefficients of \mathbf{x} projection on the $(\mathbf{v}_i)_{i=1, M}$ as $\alpha_i = \beta_i / \mu_i$.

[76] The singular values spectrum of the observation matrix \mathbf{H} is shown in descending order in Figure A1. Mostly due to the atmospheric mixing (no place is perfectly isolated from CO emissions) and also due to the precision of the computation, none of the singular values μ_i is zero. The order of magnitude of the singular values of \mathbf{H} depends on the units chosen for \mathbf{x} and \mathbf{y} , it is therefore the ratio between its largest and smallest singular values which reflects the conditioning of the least square problem. The first and last singular values in Figure A1 differ by 5 orders of magnitude. The closer to 1 the ratio is, however, the better the conditioning is. Let \mathbf{x}_0 be the solution of the system when \mathbf{H} and \mathbf{y} are perfectly known (i.e., when there are no observation or model errors). If now, \mathbf{H} and \mathbf{y} are slightly perturbed, the solution of the new system will stay close to \mathbf{x}_0 as long as the condition-

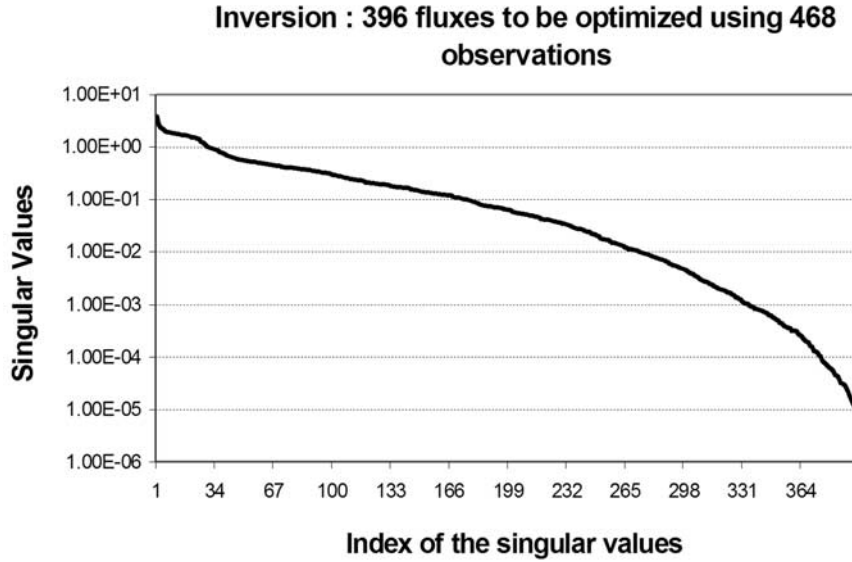


Figure A1. Singular value spectrum of the observation matrix H .

ing number is close to 1. In the present study, the conditioning number of H is about 10^5 , which is high. The existence of very small singular values is related to two factors. First of all, given the coverage of the present surface network, some sources (Africa, South America) have very little impact on the observed CO mixing ratios at the stations. The observations cannot constrain such sources. Second, the different linear combinations of sources can add up to the same total contribution at the stations. Then the sum of these sources is well constrained yet the partition between the sources is not. These two cases are reflected by the smallest singular values in the SVD spectrum of the observation matrix H . In such a case, any perturbation/error in the matrix H and/or in the observations vector can lead to a very different solution for the CO surface fluxes. When the conditioning number of a matrix is too big, it is better to truncate the spectrum $(\mu_i)_{i=1, N_x}$ and limit the problem to the optimization of a subset of parameters. To improve the conditioning number, fluxes can also be aggregated. In the present study, H was not truncated. The SVD of H gives some insight into the system properties, yet the SVD was not used, here, to compute the optimum surface fluxes. The conjunction of prior and theoretical information has been chosen because it ensures “realistic” and unique results for the solution.

Appendix B: Impact of Adding a Modeling Error to the Measurement Error in the Inversion Scheme

[77] At each station and for each month, the modeling error was taken to be half of the absolute difference between the monthly mean observed and simulated CO mixing ratios. With the modeling errors added to the observation errors, the global surface emission of CO is 1525 TgCO/yr to be compared with the 1640 TgCO/yr obtained without the modeling errors. Two thirds of the difference are due to smaller technological and biomass burning emissions in Asia. Consequently, 25% of the increase obtained during the inversion may be due to modeling errors. In future

studies, these errors will be further analyzed and taken into account.

Appendix C: Interpretation of the Analytical Expression of the Solution to the Minimization Problem

[78] The vector of a posteriori surface fluxes can be deduced in an analytical way from the statistics assumed for the problem. The two expressions below are equivalent [see *Tarantola*, 1987, pp. 70 and 158]:

$$\begin{aligned} \mathbf{x}^a &= \mathbf{x}^b + [\mathbf{H}^T \mathbf{R}^{-1} \mathbf{H} + \mathbf{P}_b^{-1}]^{-1} \mathbf{H}^T \mathbf{R}^{-1} (\mathbf{y} - \mathbf{h}(\mathbf{x}^b)) \\ \mathbf{P}^a &= [\mathbf{H}^T \mathbf{R}^{-1} \mathbf{H} + \mathbf{P}_b^{-1}]^{-1} \end{aligned} \quad (C1)$$

$$\begin{aligned} \mathbf{x}^a &= \mathbf{x}^b + \mathbf{P}_b \mathbf{H}^T [\mathbf{H} \mathbf{P}_b \mathbf{H}^T + \mathbf{R}]^{-1} (\mathbf{y} - \mathbf{h}(\mathbf{x}^b)) \\ \mathbf{P}^a &= \mathbf{P}_b - \mathbf{P}_b \mathbf{H}^T [\mathbf{H} \mathbf{P}_b \mathbf{H}^T + \mathbf{R}]^{-1} \mathbf{H} \mathbf{P}_b \end{aligned} \quad (C2)$$

[79] Writing the contribution of a particular residual Δy_k to the change in a source x_i helps understand what drives the scheme towards the optimal solution (refer to equation (C2) above):

$$\begin{aligned} x_i^a - x_i^b &= \left([\mathbf{H}^T \mathbf{R}^{-1} \mathbf{H} + \mathbf{P}_b^{-1}]^{-1} \mathbf{H}^T \mathbf{R}^{-1} \right) (i, k) (\mathbf{y} - \mathbf{h}(\mathbf{x}^b))_k \\ &= P_{ii}^b \sum_{j=1}^{468} H_{ji} (\mathbf{P}^{-1})_{jk} \Delta y_k. \end{aligned}$$

The monthly residuals at each station are correlated with each other and with the residuals at other stations as the “covariance” matrix $\mathbf{P} = [\mathbf{H} \mathbf{P}_b \mathbf{H}^T + \mathbf{R}]$ expresses it:

$$P_{ij} = \sum_{l=1}^{396} (P_{ll}^b)^2 H_{il} H_{jl} + \delta_{ij} R_{ii}.$$

The multiplication of Δy_{kk} by \mathbf{P}^{-1} projects the residual k into normalized errors at all stations. The multiplication by

H then projects from the residuals space into the surface emissions space and the multiplication by P_b transforms the normalized error on the emissions into the “final” change in the emissions.

[80] **Acknowledgments.** The authors would like to thank David Baker, David Edwards and Guy Brasseur for useful discussions on the manuscript and P. Novelli (NOAA/CMDL) for providing the observations from the CMDL cooperative network. O. Talagrand, P. Bousquet, P. Peylin and P. Ciais are to be thanked for fruitful discussions on inverse techniques. The authors also appreciate the helpful suggestions provided by two anonymous reviewers. The work of G.P., B.K. and J.F.L. is in part supported by the EOS Interdisciplinary Science Program (EOS/IDS) via grant proposal “A Study of Tropospheric Budgets of CO and CH₄ Using Data Assimilation.” The work of C.G. and G.P. is in part supported by the European Commission under the POET project (contract EVK2-1999-00011), by the Program Gestion et Impacts du Changement Climatique of the French Ministry of Environment and by the French National Program for Atmospheric Chemistry (PNCA). The work of J.F.M. is in part supported by a grant of the Belgian Office for Scientific, Technological and Cultural Affairs (OSTC). The National Center for Atmospheric Research is sponsored by the National Science Foundation.

References

- Baker, D. F., Sources and sinks of atmospheric CO₂ estimated from batch least squares inversions of CO₂ concentrations measurements, Ph.D. thesis, Princeton Univ., Princeton, N.J., 2001.
- Bates, T. S., K. C. Kelly, J. E. Johnson, and R. H. Gammon, Regional and seasonal variations in the flux of oceanic carbon monoxide to the atmosphere, *J. Geophys. Res.*, **100**, 23,093–23,101, 1995.
- Bekki, S., K. S. Law, and J. A. Pyle, Effect of ozone depletion on CH₄ and CO concentrations, *Nature*, **371**, 595–597, 1994.
- Bergamaschi, P., R. Hein, C. A. M. Brenninkmeijer, and P. J. Crutzen, Inverse modeling of the global CO cycle, 1, Inversion of CO mixing ratios, *J. Geophys. Res.*, **105**, 1909–1945, 2000a.
- Bergamaschi, P., R. Hein, C. A. M. Brenninkmeijer, and P. J. Crutzen, Inverse modeling of the global CO cycle, 2, Inversion of ¹³C/¹²C and ¹⁸O/¹⁶O isotope ratios, *J. Geophys. Res.*, **105**, 1929–1946, 2000b.
- Bousquet, P., P. Ciais, P. Peylin, M. Ramonet, and P. Monfray, Inverse modeling of annual atmospheric CO₂ sources and sinks, 1 Methods and control inversion, *J. Geophys. Res.*, **104**, 26,161–26,178, 1999a.
- Bousquet, P., P. Ciais, P. Peylin, M. Ramonet, and P. Monfray, Inverse modeling of annual atmospheric CO₂ sources and sinks, 2 Sensitivity study, *J. Geophys. Res.*, **104**, 26,179–26,193, 1999b.
- Brasseur, G. P., J. J. Orlando, and G. S. Tyndall, *Atmospheric Chemistry and Global Change*, 654 pp., Oxford Univ. Press, New York, 1999.
- Chang, M. E., D. E. Hartley, C. Cardelino, and W.-L. Chang, Inverse modeling of biogenic isoprene emissions, *Geophys. Res. Lett.*, **23**, 3007–3010, 1996.
- Chang, M. E., D. E. Hartley, C. Cardelino, D. E. Haas-Laursen, and W.-L. Chang, On using inverse methods for resolving emissions with large spatial inhomogeneities, *J. Geophys. Res.*, **102**, 16,023–16,036, 1997.
- Cicerone, R. J., How has the atmospheric concentration of CO changed, in *The Changing Atmosphere*, edited by F. S. Rowland and I. S. A. Isakson, pp. 49–61, John Wiley, New York, 1988.
- Clerbaux, C., J. Hadji-Lazarou, D. Hauglustaine, G. Megie, B.V. Khatatov, and J.-F. Lamarque, Assimilation of carbon monoxide measured from satellite in a three-dimensional chemistry-transport model, *J. Geophys. Res.*, **106**, 15,385–15,394, 2001.
- Costen, R. C., G. M. Tenneville, and J. S. Levine, Cloud pumping in a one-dimensional model, *J. Geophys. Res.*, **93**, 15,941–15,954, 1988.
- Drummond, J. R., Measurements of Pollution in the Troposphere (MOPITT), in *The Use of EOS for Studies of Atmospheric Physics*, pp. 1269–1284, North-Holland, New York, 1992.
- Dwyer, E., and J. M. Gregoire, A global analysis of vegetation fires using satellites images: Spatial and temporal dynamics, *Ambio*, **27**, 175–181, 1998.
- Enting, I., Inverse problems in atmospheric constituent studies, III, Estimating errors in surface sources, *Inverse Probl.*, **9**, 649–665, 1993.
- Enting, I. G., C. M. Trudinger, and R. J. Francey, A synthesis inversion of the concentration and D13C of atmospheric CO₂, *Tellus, Ser. B*, **47**, 35–52, 1995.
- Erickson, D. J., Ocean to atmosphere carbon monoxide flux: Global inventory and climate implications, *Global Biogeochem. Cycles*, **3**, 305–314, 1989.
- Galanter, M., H. Levy, and G. R. Carmichael, Impacts of biomass burning on tropospheric CO NO_x and O-3, *J. Geophys. Res.*, **105**, 6633–6653, 2000.
- Gelb, A., *Applied Optimal Estimation*, 374 pp., Anal. Sci. Corp., MIT Press, Cambridge, Mass., 1974.
- Gilliland, A., and P. J. Abbitt, A sensitivity study of the discrete Kalman filter (DKF) to initial condition discrepancies, *J. Geophys. Res.*, **106**, 17,939–17,952, 2001.
- Graedel, T., and P. Crutzen, L'état de l'atmosphère, *Dossier L'Atmosphère, Dossier Hors-Serie, Pour la Science*, 129 pp., 1996.
- Granier, C., G. Pétron, J.-F. Müller, and G. Brasseur, The impact of natural and anthropogenic hydrocarbons on the tropospheric budget of carbon monoxide, *Atmos. Environ.*, **34**, 5255–5270, 2000a.
- Granier, C., J.-F. Müller, and G. Brasseur, The impact of biomass burning on the global budget of ozone and ozone precursors, in *Biomass Burning and Its Inter-Relationships With the Climate System*, edited by J. L. Innes, M. Beniston, and M. M. Verstracke, pp. 69–85, Kluwer Acad., Norwell, Mass., 2000b.
- Guenther, A., P. Zimmermann, P. Harley, R. Monson, and R. Fall, Isoprene and monoterpene emission rate variability: Model evaluation and sensitivity analysis, *J. Geophys. Res.*, **98**, 12,609–12,617, 1993.
- Guenther, A., et al., A global model of natural volatile organic compound emissions, *J. Geophys. Res.*, **100**, 8873–8892, 1995.
- Haan, D., P. Martinierie, and D. Raynaud, Ice core data of atmospheric carbon monoxide over Antarctica and Greenland during the last 200 years, *Geophys. Res. Lett.*, **23**, 2235–2238, 1996.
- Haas-Laursen, D. E., D. E. Hartley, and R. G. Prinn, Optimizing an inverse method to deduce time-varying emissions of trace gases, *J. Geophys. Res.*, **101**, 22,823–22,831, 1996.
- Haine, T., The oceanic inverse problem, paper presented at Third Oxford/RAL Spring School in Quantitative Earth Observation, Nat. Environ. Res. Council, Oxford, England, March 2001.
- Hao, W. M., and M. H. Liu, Spatial and temporal distribution of tropical biomass burning, *Global Biogeochem. Cycles*, **8**, 495–503, 1994.
- Hartley, D., and R. Prinn, Feasibility of determining surface emissions of trace gases using an inverse method in a three dimensional chemical transport model, *J. Geophys. Res.*, **98**, 5183–5198, 1993.
- Heimann, M., The global atmospheric tracer model TM2, *Tech. Rep. 10*, Max-Planck-Inst. für Meteorol., Hamburg, Germany, 1996.
- Hein, R., and M. Heimann, Determination of global scale emissions of atmospheric methane using an inverse modeling technique, in *Non-CO₂ Greenhouse Gases*, pp. 271–281, Kluwer Acad., Norwell, Mass., 1994.
- Holloway, T., H. Levy II, and P. Kasibhatla, Global distribution of carbon monoxide, *J. Geophys. Res.*, **105**, 12,123–12,147, 2000.
- Houghton, J. T., Y. Ding, D. J. Griggs, N. Noguer, P. J. van der Linden, X. Dai, K. Maskell, and C. A. Johnson, *Climate Change 2001: The Scientific Basis*, Cambridge Univ. Press, New York, 2001.
- Houweling, S., T. Kaminski, F. Dentener, J. Lelieveld, and M. Heimann, Inverse modeling of methane sources and sinks using the adjoint of a global transport model, *J. Geophys. Res.*, **104**, 26,137–26,160, 1999.
- Houweling, S., F. Dentener, J. Lelieveld, B. Walter, and E. Dlugokencky, The modeling of tropospheric methane: How well can point measurements be reproduced by a global model?, *J. Geophys. Res.*, **105**, 8981–9002, 2000.
- Kaminski, T., M. Heimann, and R. Giering, A coarse grid three dimensional global inverse model of the atmospheric transport, 1, Adjoint model and Jacobian matrix, *J. Geophys. Res.*, **104**, 18,535–18,553, 1999a.
- Kaminski, T., M. Heimann, and R. Giering, A coarse grid three dimensional global inverse model of the atmospheric transport, 2, Inversion of the transport of CO₂ in the 1980s, *J. Geophys. Res.*, **104**, 18,555–18,581, 1999b.
- Kanakidou, M., and P. J. Crutzen, The photochemical source of carbon monoxide: Importance, uncertainties and feedbacks, *Chemosphere Global Change Sci.*, **1**, 91–109, 1999.
- Kanakidou, M., et al., 3D global simulations of tropospheric CO distributions: Results of the GIM/IGAC intercomparison 1997 exercise, *Chemosphere Global Change Sci.*, **1**, 263–282, 1999.
- Khalil, M. A. K., and R. A. Rasmussen, Global decrease in atmospheric carbon monoxide concentration, *Nature*, **370**, 639–641, 1994.
- Krol, M., P. J. van Leeuwen, and J. Lelieveld, Global OH trend inferred from methylchloroform measurements, *J. Geophys. Res.*, **103**, 10,697–10,711, 1998.
- Krol, M., P. J. van Leeuwen, and J. Lelieveld, Reply, *J. Geophys. Res.*, **106**, 23,164–23,519, 2001.
- Lamarque, J.-F., G. Brasseur, P. Hess, and J.-F. Müller, Three dimensional study of the relative contributions of the different nitrogen sources in the troposphere, *J. Geophys. Res.*, **101**, 22,955–22,968, 1996.
- Lanczos, C., *Linear Differential Operators*, Van Nostrand Reinhold, New York, 1961. (Republished by Dover, Mineola, N.Y., 576 pp., 1997.)
- Logan, J. A., M. J. Prather, S. C. Wofsy, and M. B. McElroy, Tropospheric chemistry: A global perspective, *J. Geophys. Res.*, **86**, 7210–7254, 1981.

- Manning, M. R., C. A. M. Brenninkmeijer, and W. Allan, The atmospheric carbon monoxide budget of the Southern Hemisphere: Implications of $^{13}\text{C}/^{12}\text{C}$ measurements, *J. Geophys. Res.*, *102*, 10,673–10,682, 1997.
- Müller, J.-F., Geographical distribution and seasonal variation of surface emissions and deposition velocities of atmospheric trace gases, *J. Geophys. Res.*, *97*, 3787–3804, 1992.
- Müller, J.-F., Modélisation tri-dimensionnelle globale de la chimie et du transport des gaz en trace dans la troposphère, Ph.D. thesis, Belg. Inst. for Space Aeron., Brussels, 1993.
- Müller, J.-F., and G. Brasseur, IMAGES: A three-dimensional chemical transport model of the global troposphere, *J. Geophys. Res.*, *100*, 16,445–16,490, 1995.
- Müller, J.-F., and G. Brasseur, Sources of upper tropospheric HO_x : A three-dimensional study, *J. Geophys. Res.*, *104*, 1705–1715, 1999.
- Novelli, P. C., K. Masarie, P. Tans, and P. Lang, Recent changes in atmospheric carbon monoxide, *Science*, *263*, 1587–1590, 1994.
- Novelli, P. C., et al., An internally consistent set of globally distributed atmospheric carbon monoxide ratios developed using results from an intercomparison of measurements, *J. Geophys. Res.*, *103*, 19,285–19,293, 1998.
- Olivier, J. G. J., A. F. Bouwman, C. W. M. Van der Maas, J. J. M. Berdowski, C. Veldt, J. P. J. Bloos, A. J. H. Visschedijk, P. Y. J. Zandveld, and J. L. Haverlag, Description of EDGAR Version 2.0: A set of global emission inventories of greenhouse gases and ozone-depleting substances for all anthropogenic and most natural sources on a per country basis and on $1^\circ \times 1^\circ$ grid, Natl. Inst. of Public Health and the Environ. (RIVM), Bilthoven, 1996.
- Paulson, S. E., and J. H. Seinfeld, Development and evaluation of a photo-oxidation mechanism for isoprene, *J. Geophys. Res.*, *97*, 20,703–20,715, 1992.
- Peylin, P., P. Bousquet, P. Ciais, and P. Monfray, Differences of CO_2 flux estimates based on a time-independent versus time-dependent inversion method, in *Inverse Methods in Global Biogeochemical Cycles*, *Geophys. Monogr. Ser.*, vol. 114, edited by P. Kasibhatla et al., pp. 295–309, AGU, Washington, D.C., 1999.
- Pickering, K. E., Y. S. Wang, W. K. Tao, C. Price, and J.-F. Müller, Vertical distributions of lightning NO_x for use in regional and global chemical transport models, *J. Geophys. Res.*, *103*, 31,203–31,216, 1998.
- Price, C., and D. Rind, Modeling global lightning distributions in a general circulation model, *Mon. Weather Rev.*, *122*(8), 1930–1939, 1994.
- Prinn, R. G., and J. Huang, Comment on “Global OH trend inferred from methylchloroform measurements” by Marteen Krol et al., *J. Geophys. Res.*, *106*, 23,151–23,157, 2001.
- Prinn, R. G., R. F. Weiss, B. R. Miller, J. Huang, F. N. Alyea, D. M. Cunnold, P. J. Fraser, D. E. Hartley, and P. G. Simmonds, Atmospheric trends and lifetime of CH_3CCl_3 and global OH concentrations, *Science*, *129*, 187–192, 1995.
- Prinn, R. G., et al., A history of chemically and radiatively active gases in air deduced from ALE/GAGE/AGAGE, *J. Geophys. Res.*, *105*, 17,751–17,792, 2000.
- Smolarkiewicz, P. K., and G. A. Grell, A class of monotone interpolation schemes, *J. Comput. Phys.*, *101*, 431–440, 1991.
- Spivakovsky, C. M., R. Yevich, J. A. Logan, S. C. Wofsy, M. B. McElroy, and M. J. Prather, Tropospheric OH in a three-dimensional chemical tracer model: An assessment based on observations of CH_3CCl_3 , *J. Geophys. Res.*, *95*, 18,441–18,471, 1990.
- Streets, D. G., and S. T. Waldhoff, Present and future emissions of air pollutants in China: SO_2 , NO_x , and CO, *Atmos. Environ.*, *34*, 363–374, 2000.
- Talagrand, O., Assimilation of observations: An introduction, *J. Meteorol. Soc. Jpn.*, *75*(1B), 191–209, 1997.
- Tarantola, A., *Inverse Problem Theory*, Elsevier Sci., New York, 1987.
- Tarantola, A., and B. Valette, Inverse problems = quest for information, *J. Geophys. Res.*, *50*, 159–170, 1982a.
- Tarantola, A., and B. Valette, Generalized nonlinear inverse problems solved using the least squares criterion, *Rev. Geophys.*, *20*, 219–232, 1982b.
- World Meteorological Organization/United Nations Environment Programme (WMO/UNEP), *Scientific Assessment of Ozone Depletion*, *World Meteorol. Org. Global Ozone Res. and Monit. Proj. Rep.* *44*, Brussels, 1998.
- Wotawa, G., P. C. Novelli, M. Trainer, and C. Granier, Inter-annual variability of summertime CO concentrations in the Northern Hemisphere explained by boreal forest fires in North America and Russia, *Geophys. Res. Lett.*, *28*, 4575–4578, 2001.
- Wunsch, C., *The Ocean Circulation Inverse Problem*, 442 pp., Cambridge Univ. Press, New York, 1996.

J. Gille, B. Khattatov, J.-F. Lamarque, G. Pétron, and V. Yudin, Atmospheric Chemistry Division, NCAR, 1850 Table Mesa Drive, Boulder, CO 80307, USA. (gap@ucar.edu)

C. Granier, Service d'Aéronomie, Université Paris 6, 4 Place Jussieu, F-75252 Paris Cedex 05, France. (clg@aero.jussieu.fr)

J.-F. Müller, Belgian Institute for Space Aeronomy, 3, avenue Circulaire, B-1180 Brussels, Belgium. (jean-francois.muller@bira-iasb.oma.be)